J. Fluid Mech. (2023), *vol.* 975, A44, doi:10.1017/jfm.2023.828

JFM PAPERS

Effects of reverberating waves and interface coupling on a divergent Richtmyer–Meshkov instability

Duo Zhang[1], **Juchun Ding**[1,†], **Ming Li**[2], **Liyong Zou**[3] **and Xisheng Luo**[1]

[1]Advanced Propulsion Laboratory, Department of Modern Mechanics, University of Science and Technology of China, Hefei 230026, PR China

[2]Xi'an Aeronautics Computing Technique Research Institute, Xi'an 710068, PR China

[3]Laboratory for Shock Wave and Detonation Physics, Institute of Fluid Physics, China Academy of Engineering Physics, Mianyang 621900, PR China

(Received 21 May 2023; revised 24 August 2023; accepted 30 September 2023)

Shock-tube experiments on Richtmyer–Meshkov (RM) instability at a perturbed SF_6 layer surrounded by air, induced by a cylindrical divergent shock, are reported. To explore the effects of reverberating waves and interface coupling on instability growth, gas layers with various shapes are created: unperturbed inner interface and sinusoidal outer interface (case US); sinusoidal inner and outer interfaces that have identical phase (case IP); sinusoidal inner and outer interfaces that have opposite phase (case AP). For each case, three thicknesses are considered. Results show that reverberating waves inside the layer dominate the early-stage instability growth, while interface coupling dominates the late-stage growth. The influences of waves on divergent RM instability are more pronounced than the planar and convergent counterparts, which are estimated accurately based on gas dynamics theory. Both the wave influence and interface coupling depend heavily on the layer shape, leading to diverse growth rates: the quickest growth for case AP, medium growth for case US, the slowest growth for case IP. In particular, for the IP case, there exists a critical thickness below which the instability growth is suppressed by both the reverberating waves and interface coupling. This provides an efficient way to modulate the growth of divergent RM instability. It is found that divergent RM instability involves weak nonlinearity and strong interface coupling such that the linear theory of Mikaelian (*Phys. Fluids*, vol. 17, 2005, 094105) can well reproduce the instability growth at late stages for all cases. This constitutes the first experimental confirmation of the Mikaelian theory.

Key words: shock waves, shear-flow instability

[†] Email address for correspondence: djc@ustc.edu.cn

1. Introduction

Hydrodynamic instabilities such as Rayleigh–Taylor (RT) instability and Richtmyer–Meshkov (RM) instability play an important role in natural and industrial fields such as astrophysics (Abarzhi *et al.* 2019), supersonic combustion (Yang, Kubota & Zukoski 1993) and inertial confinement fusion (ICF) (Lindl *et al.* 2014). The RT instability (Rayleigh 1883; Taylor 1950) occurs when a perturbed interface separating two fluids of different densities is in a gravitational field (or an acceleration field) pointing from heavy fluid to light. The RM instability (Richtmyer 1960; Meshkov 1969) occurs when a perturbed interface between two different fluids is subjected to an impulsive acceleration, typically by a shock wave. From the loading point of view, RM instability can be viewed as an impulsive variant of RT instability. Although the two instabilities share common evolution processes, such as the formation of spike (heavy fluid penetrates into light) and bubble (light fluid rises into heavy), and the flow transition to turbulent mixing (under a certain condition), their evolution regimes are distinct. This impedes the straightforward application or extension of the knowledge of RT instability to RM instability.

Over the past decades, much attention has been paid to RM instability, and substantial progress has been achieved in theory (Richtmyer 1960; Zhang & Sohn 1997; Dimonte & Ramaprabhu 2010; Nishihara *et al.* 2010; Zhang, Deng & Guo 2018), experiment (Prestridge *et al.* 2013; Biamino *et al.* 2015; Reese *et al.* 2018; Mohaghar *et al.* 2019; Sewell *et al.* 2021) and simulation (Schilling & Latini 2010; Lombardini, Pullin & Meiron 2014; Wonga & Lelea 2017; Groom & Thornber 2021; Li *et al.* 2022*b*). The existing studies are concerned mainly with RM instability at a single interface. This is not the case for real situations, in which RM instability occurs usually at two or multiple interfaces. For example, an ICF capsule usually consists of three concentric shells – the outer ablator, the middle solid deuterium-tritium (DT) ice and the inner gaseous DT fuel – which form two material interfaces (Betti & Hurricane 2016). As the capsule is irradiated by high-power X-rays (indirect drive) or laser beams (direct drive), shock waves are generated, which subsequently propagate inwards, triggering RM instability at both the inner and outer interfaces. Also, in a supernova explosion, the stellar collapse produces a strong divergent shock, which moves outwards and passes across the multi-layer elements, inducing RM instability (Arnett *et al.* 1989). It is therefore more valuable practically to investigate RM instability at a finite-thickness fluid layer with two interfaces.

RM instability at an SF_6 layer embedded in air impacted by a planar shock wave was first realized by Jacobs *et al.* (1993) in a shock-tube experiment, and three distinct flow patterns – including the upstream mushroom, downstream mushroom and sinuous mode – were observed. The random emergence of three flow patterns in the experiment of Jacobs *et al.* (1993) was ascribed to the sensitivity of the layer evolution to its initial shape (Budzinski, Benjamin & Jacobs 1994; Jacobs *et al.* 1995). Also, Rightley *et al.* (1999) examined experimentally the evolution of a shock-accelerated gas layer with various initial perturbations, and an abrupt mixing transition was observed for a multi-mode initial perturbation. Since then, turbulent mixing developing from RM instability at a gas layer (called RM turbulence) has been investigated continually with laser-sheet imaging techniques such as particle image velocimetry and planar laser induced fluorescence. The effect of initial conditions (the layer shape, the concentration distribution, the shock strength, etc.) and the influence of reflected shock on the RM turbulence were analysed especially (Prestridge *et al.* 2000; Balakumar *et al.* 2008, 2012; Tomkins *et al.* 2008; Orlicz *et al.* 2009; Orlicz, Balasubramanian & Prestridge 2013; Tomkins *et al.* 2013). In all the above experiments, the gas layer is produced by vertically injecting a gas curtain into the test section of the shock tube through a contoured nozzle. Although the jet technique greatly facilitates the experimental study of RM instability, it brings several uncertainties into initial conditions, such as the non-uniform distribution of gas concentration inside the layer, initial velocity of the test gas in the vertical direction, three-dimensionality and gas diffusion, which could evidently influence the instability growth (Tomkins *et al.* 2008; Orlicz *et al.* 2009; Bai *et al.* 2010; Balasubramanian, Orlicz & Prestridge 2013; Shankar & Lele 2013).

Recently, a novel soap-film technique was developed to create a sharp gaseous interface with controllable shape (Liu *et al.* 2018). A series of elaborate experiments demonstrated that this technique can largely eliminate three-dimensionality and gas diffusion. In addition, the soap film was found to produce a negligible influence on the interface evolution at early to intermediate stages (Liang *et al.* 2021; Guo *et al.* 2022; Chen *et al.* 2023). More recently, this soap-film technique was extended to generate gas layers with controllable shape and thickness, which enables the experimental study on RM instability at various types of controllable gas layers (Liang & Luo 2021*a*, 2022). Experimental results showed that the reverberating waves inside the layer could induce RT instability/stability, which promotes/suppresses the instability growth. In addition, an interface coupling effect is evident (particularly for a thin layer), which significantly affects the instability growth at both interfaces of the layer (Jacobs *et al.* 1995; Mikaelian 1995, 2005). The soap-film technique was also developed to generate gas layers in the test section of a semi-annular convergent shock tube, with which a series of experiments on convergent RM instability at a perturbed gas layer were realized (Ding *et al.* 2019; Li *et al.* 2020*a*, 2022*a*; Sun *et al.* 2020). Convergent RM instability is more complex than the planar counterpart due to the existence of a geometric convergence effect and reshock (Bell 1951; Plesset 1954; Epstein 2004). Also, the shocked interface is decelerated when it approaches the geometric centre, inducing RT instability/stability (Ding *et al.* 2017*b*). These new regimes could couple with interface coupling and wave influence, providing more possibilities and complexities for the growth of convergent RM instability at a gas layer.

The existing studies were limited to RM instability induced by planar and convergent shocks. So far, RM instability at a gas layer induced by a divergent shock (i.e. divergent RM instability) has rarely been investigated, although it is equally important in nature and applications. For example, divergent RM instability is an important physical process in supernova explosion (Kuranz *et al.* 2018; Abarzhi *et al.* 2019). Also, in ICF, after the convergent shock focuses at the geometric centre, a divergent shock is generated immediately (i.e. the reshock is a divergent shock), which later moves outwards and interacts with the material interfaces, greatly enhancing the material mixing (i.e. reducing the energy yield). The underlying regimes of divergent RM instability are distinctly different from the planar or convergent case. Specifically, a divergent shock becomes weaker and weaker with time, thus a non-uniform, unsteady pressure field is established behind it, which leads to interface deceleration (i.e. RT stability/instability) (Li *et al.* 2020*b*; Zhang *et al.* 2023). Also, for a gas layer moving in a divergent geometry, the layer becomes progressively thinner with time due to geometric divergence and thus exhibits an increasingly strong interface coupling effect (Zhang *et al.* 2023). Moreover, for divergent RM instability, nonlinearity and compressibility are much weaker than those of convergent RM instability (Li *et al.* 2020*b*). It is therefore highly desirable to perform elaborate experiments on divergent RM instability at a gas layer with various shapes and thicknesses, which can facilitate elucidating the underlying regimes of divergent RM instability.

A gas layer could present four configurations in terms of shape: sinusoidal inner interface and unperturbed outer interface (configuration I); unperturbed inner interface and sinusoidal outer interface (configuration II); sinusoidal inner and outer interfaces that present the same phase (configuration III); sinusoidal inner and outer interfaces that present opposite phases (configuration IV). Divergent RM instability at a gas layer of configuration I has been examined by Zhang *et al.* (2023) in a specially designed divergent shock tube. It was found that reverberating waves inside the layer produce influences on the instability growth that are more pronounced than those of planar and convergent RM instabilities. Also, interface coupling produces a significant influence on the outer interface development, but a weak influence on the inner interface evolution. In this study, we will consider the evolutions of gas layers in the remaining three configurations (II, III and IV). It should be noted that the phase difference between the two interfaces of the layer not only results in different interface coupling effect, but also induces a different shape of the reverberating waves such that the wave effect will also be distinct. By comparing the experimental result among different configurations, effects of reverberating waves and interface coupling will be revealed and then analysed. The main factors dominating the gas layer evolution at the early and late stages are elucidated in detail. Rich experimental data for various types of gas layers obtained in this work provide the first opportunity to fully examine the validity of the linear theory of Mikaelian (2005). The present work together with that of Zhang *et al.* (2023) will constitute a systematic study of divergent RM instability at a perturbed heavy gas layer.

2. Experimental methods

The experiments are carried out in a divergent shock tube that is designed based on shock dynamics theory. Benefiting from the elaborately designed wall profiles that realize the planar-convergent–planar-divergent shock transformations, an initial planar shock can be transformed gradually to a cylindrical divergent shock. The design principle of the curved walls and the structure of the shock tube have been detailed in previous studies (Zhai *et al.* 2010; Zhan *et al.* 2018; Li *et al.* 2020*b*). A sketch of the curved part of the shock tube executing the planar-convergent–planar-divergent shock transformations is shown in figure 1(*a*) (not drawn to scale). The curved part has designed length 2100.0 mm (the whole shock tube is 6400.0 mm long) and inner height 7.0 mm, and its left-hand end is connected to the driven section. In experiment, a planar shock of Mach number 1.35 is generated immediately after the rupture of the diaphragm separating the driver and driven sections. When this planar shock propagates along the concave wall *AB*, it is gradually transformed to a cylindrical convergent shock. As time proceeds, the cylindrical shock implodes along the oblique wall *BC*, with its strength being augmented progressively. Later, it is converted back into a planar shock by the convex wall *CD*. This planar shock has Mach number 1.71, namely, it is stronger than the initial planar shock. Finally, the intensified planar shock is converted to a cylindrical divergent shock by the convex wall *EF*. Afterwards, the divergent shock propagates outwards and collides with the downstream SF_6 layer surrounded by air, triggering divergent RM instability. Since a divergent shock becomes weaker and weaker with time, it should be relatively strong at the beginning. An advantage of the present design is to intensify the initial planar shock, which is essential for producing a divergent shock with a certain strength. Compared to a rectangular cross-section with the same inner dimension as the throat of the present shock tube, the present design can produce a stronger planar shock under the same pressure ratio between the driver and driven sections.

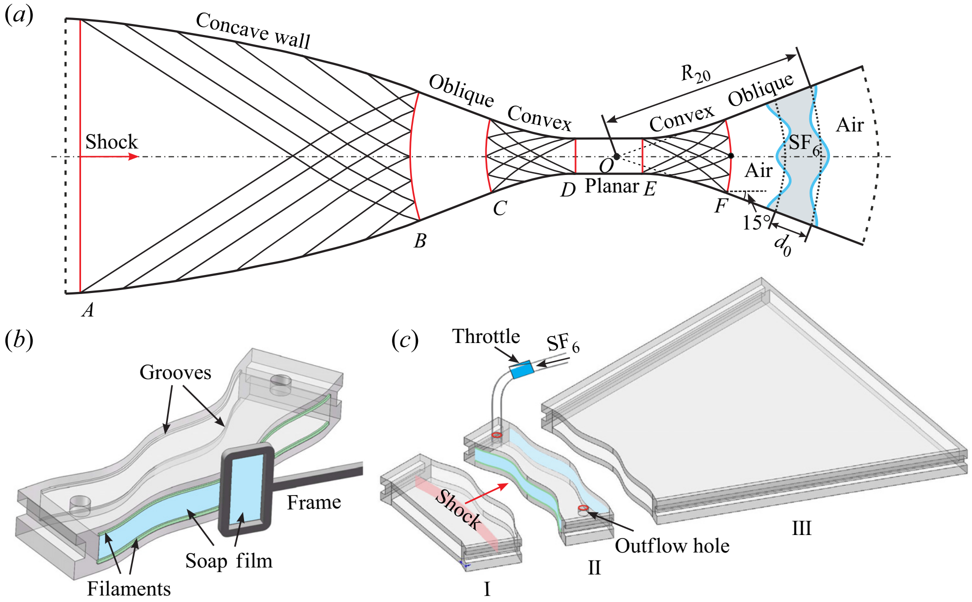

Figure 1. (*a*) Sketch of the curved part of the divergent shock tube. (*b*) An enlarged view of section II of the interface-formation device. (*c*) A drawing of the interface-formation device.

A soap film is a natural material to separate two different gases, which has a negligibly weak influence on the flow. Owing to surface tension, it is difficult to generate a soap film of a desired shape without any constraint or support. Recent studies have shown that thin filaments can be used to constrain the soap film, changing its shape (Liu *et al.* 2018; Li *et al.* 2020*b*; Liang & Luo 2021*b*). This provides a novel way to generate soap-film interfaces of desired shapes. In this work, we use such a technique to generate gas layers with controllable shapes and thicknesses. As illustrated in figure 1(*c*), the gas layer is formed in a device composed of sections I, II and III. These three sections are made up of transparent acrylic plates (3.0 mm thick) sculpted by a high-precision engraving machine. Four grooves (0.75 mm thick and 0.5 mm wide) with the same shapes as the boundaries of the desired gas layer are engraved on the internal surfaces of the upper and lower plates of section II. Then four thin filaments (1.0 mm thick and 0.5 mm wide) with the same shapes as the grooves are respectively inserted into the four grooves to produce the constraints. The filaments protruding into the flow field are less than 0.3 mm in height and thus produce a negligible influence on the flow (Wang *et al.* 2022). As shown in figure 1(*b*), when a square frame dipped with a moderate amount of soap solution (60 % distilled water, 20 % sodium oleate and 20 % glycerin) is pulled along the filaments on both sides of section II, a gas layer with two soap-film boundaries is formed immediately. Then SF_6 gas is pumped into the layer through an inflow hole, and meanwhile air is exhausted through an outflow hole, as shown in figure 1(*c*). In this way, an SF_6 layer surrounded by air is created. Note that the thin filaments can prevent the soap film from shrinking and sliding into section II, thus the layer shape can be maintained for a certain period of time. An oxygen concentration detector is placed at the outflow hole to monitor the oxygen concentration of the gas mixture exhausted from the layer. When the measured oxygen concentration reaches the experimental requirement (below 2 %), the inflow and outflow holes are sealed immediately. Then the drawer containing sections I, II and III is inserted quickly into the test section, and the experiment can be conducted. Note that the initial conditions of the present experiments, including the shock Mach number, the gas layer shape and the gas concentration, can be well controlled, which ensures a high repeatability of the experimental results.

In this work, the gas layer interface with a smaller radius is defined as the inner interface, and the other one as the outer interface. In a cylindrical coordinate system, the inner/outer interface can be parametrized as $r_i = R_{i0} + a_{i0}\cos(n\theta - \pi)$ (where $i = 1, 2$ refer to the inner and outer interfaces, respectively), where R_{i0} stands for the radius of the initial interface ($R_{10} = 150$ mm, $R_{20} = 160$, 170, 180 mm, corresponding to the layer thicknesses $d_0 = 10$, 20, 30 mm), θ is the azimuthal angle, and a_{i0} is the initial amplitude. In experiment, the interface amplitude (defined as half of the distance between crest and trough) is measured by identifying accurately the positions of the crest and trough. If the crest and trough are attached to the wall of the test section, then their movements would be influenced by the boundary layer. To avoid the influence of the boundary layer on the accuracy of the measured amplitude, the initial single-mode interface should present at least two wavelengths in the V-shaped test section. Since the V-shaped test section has angle 30°, the azimuthal mode number should be $n \geq 24$. On the other hand, the larger n, the greater the surface tension of the sinusoidal soap film, which brings a greater challenge to the property of the soap solution. Thus in experiment it is hard to generate a sinusoidal soap film with very large azimuthal mode number. For these considerations, $n = 24$ is adopted in this work. The flow field is recorded by a high-speed schlieren system that consists of a high-speed video camera (FASTCAM SAZ, Photron Ltd), a DC stabilized light source (DCRIII, SCHOTT North America, Inc.) and multiple optical lens groups. The frame rate of the high-speed camera is set to be 60 000 f.p.s., with exposure time 1 μs. The spatial resolution of the schlieren images is 0.29 mm pixel^{-1}. The ambient pressure and temperature are approximately 101.3 kPa and 294 ± 1 K, respectively.

3. Results and discussions

3.1. *Background flow*

The background flow of divergent RM instability is more complicated than the planar counterpart due to the presence of geometric divergence and an unsteady, non-uniform pressure field behind the divergent shock, for which there is no theoretical solution. Thus quasi-one-dimensional (quasi-1-D) experiments corresponding to an unperturbed SF_6 layer surrounded by air impacted by a divergent shock are required to examine the background flow. Fortunately, these quasi-1-D experiments have been reported recently by Zhang *et al.* (2023). A sequence of schlieren images (upper) and schematic diagrams (lower) illustrating the evolution of the SF_6 layer driven by a cylindrical divergent shock are given in figure 2. The time origin here is defined as the moment at which the incident shock encounters the initial inner interface. At the beginning, an incident cylindrical shock (ICS) moves outwards and then collides with the inner interface (II_1) of the layer, bifurcating into an inward-moving reflected shock (RS_1) and an outward-moving transmitted shock (TS_1). After that, the shocked inner interface (SI_1) moves downstream and gradually leaves its original position. Due to shock impact, the soap film atomizes into small droplets, causing the thickening of SI_1 in schlieren images (122 μs). The relationship between the size of the atomized soap droplets and the incident shock strength has been investigated by Cohen (1991) and Ranjan *et al.* (2008). According to their work, the soap droplets are estimated to be approximately 30 μm in radius for the present experiments,

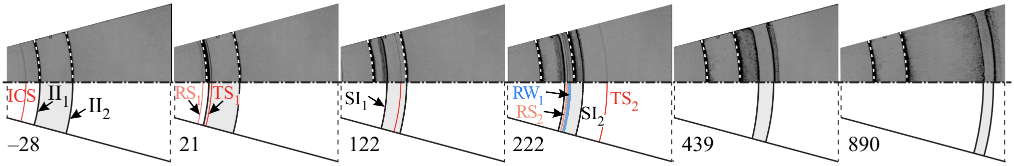

Figure 2. Schlieren images (upper) and schematic diagrams (lower) showing the developments of wave patterns and interfacial morphologies for an unperturbed SF$_6$ layer with $d_0 = 30$ mm accelerated by a cylindrical divergent shock. The white dotted lines indicate the thin filaments used to form the initial soap-film interfaces; ICS is the incident cylindrical shock; II$_i$ is the initial interface ($i = 1, 2$ refer to the inner and outer interfaces, respectively); SI$_i$ is the shocked interface; TS$_j$ is the jth transmitted shock; RS$_j$ is the jth reflected shock; RW$_1$ is the first rarefaction wave reflected from the outer interface. The unit of numbers is μs.

in which the incident shock Mach number is $M_i \approx 1.3$. Previous experiments with such a soap-film technique showed that the experimental results are in good agreement with numerical simulations and theoretical predictions (Wang, Si & Luo 2013; Ding *et al.* 2017*a*; Liu *et al.* 2018), which indicates a negligible influence of soap droplets on the interface evolution. Later, the outgoing TS$_1$ collides with the initial outer interface (II$_2$) of the layer, splitting into a second transmitted shock (TS$_2$) and an inward-moving rarefaction wave (RW$_1$). Note that a weak reflected shock (RS$_2$) is produced during this process, which is caused by the interaction of TS$_1$ with the protruding filaments. This reflected shock has also been observed in previous experiments, and its influence on the instability development was demonstrated to be negligible (Vandenboomgaerde *et al.* 2018; Liang *et al.* 2020*a*). Later, RW$_1$ accelerates the inner interface, and an outward-moving compression wave (CW$_1$) is immediately generated inside the layer (not visible in schlieren images due to the weak intensity). Afterwards, CW$_1$ compresses and accelerates the outer interface, generating a second rarefaction wave (RW$_2$), which later interacts with the inner interface again. The above wave propagation process would be repeated many times inside the layer until the reverberating waves are negligibly weak. In this work, after CW$_1$ passes across the outer interface, the waves reverberating inside the gas layer are very weak and can be ignored. The white dotted lines in figure 2 indicate the protruding filaments used to constrain the initial soap-film interfaces. A unique feature of the motion of the gas layer in a divergent geometry is that the layer becomes thinner and thinner with time due to geometric divergence, and thus exhibits an increasingly strong interface coupling effect, which will be discussed later. The inner and outer interfaces maintain a nearly cylindrical shape during the experimental time, which indicates a limited influence of boundary layer on the interface motion.

A detailed analysis on the background flow of divergent RM instability has been reported by Zhang *et al.* (2023), and the main results are summarized below. The inner and outer interfaces of the layer move uniformly at the early stage, and their velocities can be influenced by the reverberating waves inside the layer. At late stages, the two interfaces decelerate, evidently due to the combined effects of geometric divergence and a non-uniform pressure field behind the divergent shock. The dimensionless displacements of the inner (outer) interface for gas layers of different thickness collapse well from early to late stages. A general 1-D theory applicable to an arbitrary-thickness layer is developed by taking the non-uniform pressure distribution and geometric divergence into account, which gives a good prediction of the motion of the shocked unperturbed layer in divergent geometry. For the details of the 1-D theory, readers are referred to the work of Zhang *et al.* (2023). The background flow described here would facilitate the analysis and understanding of the evolution of a perturbed gas layer.

Case	d_0	a_{10}	a_{20}	V_{ics}	V_{ts_1}	V_{ts_2}	ΔV_1	ΔV_2	mfra(SF_6)	A	A^+
d10-UU	10	0	0	432.2	207.4	409.9	97.6	116.7	0.93	0.61	0.65
d20-UU	20	0	0	432.4	207.3	403.1	96.7	111.4	0.95	0.61	0.65
d30-UU	30	0	0	432.6	204.2	408.3	96.7	110.9	0.96	0.62	0.66
d10-US	10	0	2	432.2	215.6	414.4	95.5	117.0	0.92	0.58	0.62
d20-US	20	0	2	432.4	208.3	412.4	95.7	113.8	0.94	0.61	0.64
d30-US	30	0	2	432.6	207.8	408.3	95.1	108.3	0.95	0.61	0.65
d10-IP	10	2	2	432.3	210.1	403.7	96.9	110.9	0.94	0.60	0.64
d20-IP	20	2	2	432.6	208.5	408.1	98.0	111.4	0.94	0.61	0.65
d30-IP	30	2	2	432.2	202.4	406.1	94.3	104.5	0.96	0.63	0.66
d10-AP	10	2	-2	432.2	213.2	412.3	97.7	119.6	0.93	0.59	0.63
d20-AP	20	2	-2	432.5	212.8	418.7	97.8	108.8	0.93	0.59	0.63
d30-AP	30	2	-2	433.2	204.7	404.6	94.4	106.8	0.96	0.62	0.66

Table 1. Here, d_0 is the initial thickness of the layer, a_{10} (a_{20}) is the initial amplitude of the inner (outer) interface, V_{ics} is the velocity of the ICS, V_{ts_j} is the velocity of the jth transmitted shock, ΔV_1 (ΔV_2) is the post-shock velocity of the inner (outer) interface, mfra(SF_6) refers to the mass fraction of SF_6 inside the gas layer A (A^+) to the pre-shock (post-shock) Atwood number. The amplitude and thickness are in mm, the velocity is in m s^{-1}.

3.2. *Evolution of a perturbed gas layer*

Quasi-two-dimensional (quasi-2-D) experiments, corresponding to nine types of SF_6 layers with various thicknesses, amplitudes and phases of the inner and outer interfaces impacted by a cylindrical divergent shock, are performed. Specifically, three thicknesses are considered: the inner interface is fixed at $R_{10} = 150$ mm, and the outer interface takes radii $R_{20} = 160, 170, 180$ mm corresponding to the layer thicknesses $d_0 = 10, 20, 30$ mm, respectively. For each thickness, various amplitudes and phases of the inner and outer interfaces are taken: case US ($a_{10} = 0$ mm, $a_{20} = 2$ mm), case IP ($a_{10} = a_{20} = 2$ mm) and case AP ($a_{10} = 2$ mm, $a_{20} = -2$ mm). Here, the symbol US means that the inner interface is unperturbed while the outer interface is sinusoidally perturbed; IP means that there exist two in-phase single-mode perturbations at the inner and outer interfaces, respectively; AP means that there exist two anti-phase perturbations at the inner and outer interfaces, respectively. It should be mentioned that case SU ($a_{10} = 2$ mm, $a_{20} = 0$ mm, i.e. the inner interface is sinusoidally perturbed while the outer interface is unperturbed) has been examined in our recent work (Zhang *et al.* 2023) and is not repeated here. An unperturbed gas layer is denoted by case UU. For the convenience of expression, in this work a gas layer is named as case d10/20/30-SU/US/IP/AP, in which the first symbol denotes the layer thickness, and the second denotes the layer shape. Detailed parameters corresponding to the initial conditions for each case are listed in table 1, where the Atwood number is defined as $A = (\rho_2 - \rho_1)/(\rho_2 + \rho_1)$, with ρ_2 and ρ_1 being the gas densities inside and outside the layer, respectively. As we can see, the parameters of the perturbed layers are nearly equal to those of the unperturbed layers.

A key parameter in the experiment is the mass fraction of SF_6 inside the layer, which determines the instability growth rate at both interfaces. Although a gas concentration detector is used to measure the oxygen concentration of the gas mixture exhausted from the outflow hole, it can ensure only a high concentration of SF_6 inside the layer rather than measuring directly the mass fraction of SF_6. In this work, we estimate the mass fraction of SF_6 inside the layer using the following method. For a planar shock impacting a flat light/heavy interface, a 1-D flow that is composed of four uniform regions separated by a reflected shock, a transmitted shock and a contact surface, is produced. According to 1-D gas dynamics theory, we can establish the relations between the flow parameters on both sides of the reflected and transmitted shocks. With the compatibility relation at the contact surface (i.e. velocity and pressure continuity), the following equation can be derived:

$$\left[\frac{(\varLambda_2-1)\,\rho_1}{(\varLambda_1-1)\,\rho_2}\right]^{1/2}\frac{P_t-1}{(P_t\varLambda_2+1)^{1/2}}=\frac{P_i-1}{(P_i\varLambda_1+1)^{1/2}}-\left(\frac{\rho_1}{\rho_1'}\right)^{1/2}\frac{P_t-P_i}{(P_t\varLambda_1+P_i)^{1/2}},\tag{3.1}$$

where

$$\left.\begin{aligned}\varLambda_1&=(\gamma_1+1)/(\gamma_1-1),\\ \varLambda_2&=(\gamma_2+1)/(\gamma_2-1),\\ P_i&=1+2\gamma_1/(\gamma_1+1)(M_i^2-1),\\ \rho_1/\rho_1'&=[(\gamma_1-1)M_i^2+2]/[(\gamma_1+1)M_i^2].\end{aligned}\right\}\tag{3.2}$$

Here, γ_1 (γ_2) refers to the specific heat ratio inside the layer, P_i (P_t) to the pressure ratio across the incident shock (transmitted shock), ρ_1' to the fluid density behind the incident shock, and M_i to the Mach number of the incident shock. In experiment, the gas outside the layer is pure air. The velocity of the incident shock is measured just before it collides with the inner interface, then the corresponding M_i is calculated. The mass fraction of SF_6 is obtained by iterative method via numerical calculation. Specifically, specifying an arbitrary initial value between 0 and 1 for the mass fraction of SF_6 inside the layer, the flow parameters inside the layer (e.g. ρ_2 and γ_2) can be obtained. Substituting the known parameters into (3.1), the pressure ratio across the transmitted shock (P_t) can be solved, and then the strength of the transmitted shock is available. If the calculated strength of the transmitted shock is stronger than the measured one, then the value of the mass fraction is reduced; otherwise, it is increased. This process is repeated many times until the calculated value is in good agreement with the measured one (i.e. their difference is below 0.1 %). For the unperturbed layer with $d_0 = 30$ mm, the mass fraction of SF_6 inside the layer is calculated to be 96 %. With this value, the flow velocity behind TS_1 is calculated to be 92.0 m s^{-1} based on 1-D gas dynamics theory, which agrees reasonably with the experimental measurement (96.7 ± 1.0 m s^{-1}). This demonstrates good reliability of the present calculation method. Also, it indicates a negligible influence of soap droplets on the flow.

Developments of the wave patterns and interface morphologies illustrated by sequences of schlieren images for all cases are displayed in figure 3. Here, we take case d20-US as an example to detail the evolution process. At the beginning (−7 μs), an ICS together with an unperturbed inner interface II_1 and a sinusoidal outer interface II_2 are observed clearly, which demonstrates good feasibility of the present experimental method. The velocity of the ICS is measured to be $V_{ics} = 432.4$ m s^{-1} just before it collides with the inner interface, corresponding to $M_i = 1.25$. After the ICS collides with the fast/slow inner interface, it immediately bifurcates into an upstream-moving reflected shock RS_1 and a downstream-moving transmitted shock TS_1. Note that the fast/slow interface refers to an A/B interface where the sound speed of gas A is larger than that of gas B (Samtaney, Ray & Zabusky 1998). After that, the shocked inner interface SI_1 moves outwards at initial velocity $\Delta V_1 \approx 95.7$ m s^{-1}. As time proceeds, it maintains a cylindrical shape with no instability due to the complete alignment of ICS with the initial interface.

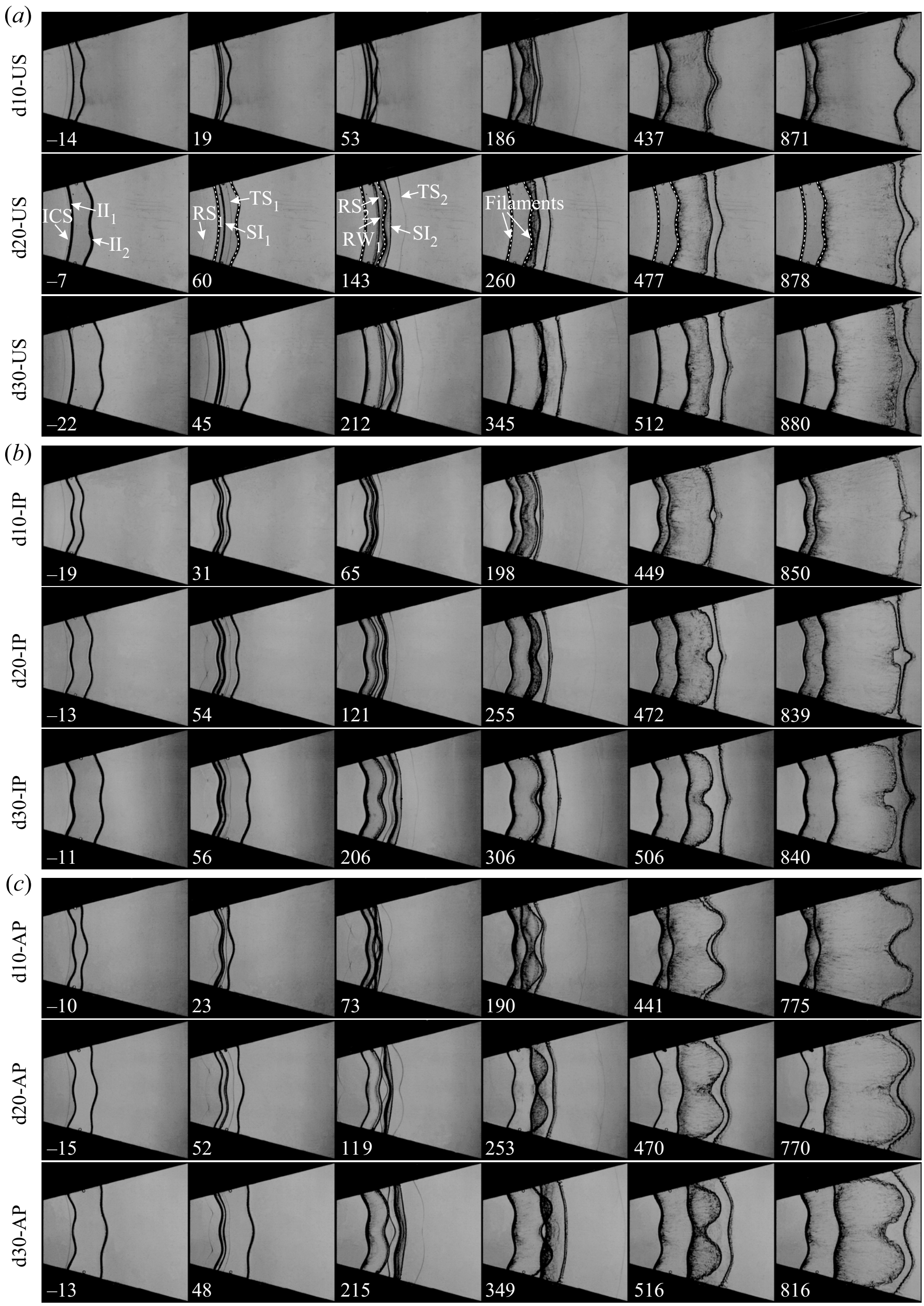

Figure 3. Schlieren images showing the developments of wave patterns and interfacial morphologies for all cases. The white dotted lines indicate the thin filaments used to form the initial soap-film interfaces. The symbols are the same as those in figure 2. The unit of numbers is μs.

Afterwards, the cylindrical TS_1 collides with the sinusoidal outer interface, immediately bifurcating into a second transmitted shock TS_2 and an upstream-moving rarefaction wave RW_1 (143 μs). Note that RW_1 possesses an identical perturbation phase relative to the outer interface, while TS_2 presents an opposite phase. After the impact of TS_1, the amplitude of the outer interface reduces gradually to zero (i.e. phase reversal) and then increases gradually with an opposite phase. Later, the disturbed RW_1 stretches and accelerates the inner interface, seeding a visible perturbation on the inner interface (260 μs). It indicates that for a heavy gas layer, the initial perturbation of the outer interface can be transferred to the unperturbed inner interface through RW_1. This differs from the SU case, where the unperturbed outer interface suffers a negligible influence of reverberating waves and thus maintains a nearly cylindrical shape during a long period of time (Zhang *et al.* 2023). During the interaction of RW_1 with the inner interface, an outward-moving compression wave CW_1 is generated (not visible schlieren images due to the weak intensity), which later compresses and accelerates the shocked outer interface SI_2. At late times, the inner and outer interfaces increase in amplitude with an identical phase (477–878 μs). The time origin for the evolution of a perturbed layer is defined as the moment at which the incident shock arrives at the mean position of the inner interface.

For case d20-IP, the rarefaction wave RW_1 is in phase with the inner interface, thus their interaction lasts a relatively shorter period of time. As a result, RW_1 stretches (or amplifies) the inner interface amplitude to a lesser extent than in case d20-US, which is confirmed by the quantitative data hereinafter. After the impact of TS_1, the outer interface first reverses phase, and then presents an anti-phase perturbation relative to the inner interface. For this case, interface coupling inhibits the instability growth at each interface according to Mikaelian (1985, 1995). For case d20-AP, RW_1 is out of phase with the inner interface and thus takes a longer period of time to passes across the inner interface. As a result, it stretches (or amplifies) the inner interface amplitude to a larger extent than the IP and US cases (253 μs). Also, after phase reversal, the outer interface presents an in-phase perturbation relative to the inner interface. For this case, interface coupling promotes the instability growth at each interface of the layer. This explains reasonably the observation that the instability growth in the AP case is quicker than in the IP and US cases (770 μs). It manifests that the phase difference between the two interfaces significantly affects the instability growth at a gas layer. The interface contours at typical moments for the IP, AP and US cases with thickness 20 mm are extracted from the experimental schlieren images with a post-processing program written in MATLAB language, as shown in figure 4. This makes it much easier to assess the phase difference between the two interfaces on the layer evolution. Results of various layer thicknesses show that the layer thickness produces an evident influence on the growth rate of the instability at each interface, but cannot alter the eventual perturbation phases of the two interfaces. For all nine cases, the gas layer becomes thinner and thinner with time due to geometric divergence. In particular, the inner and outer interfaces coalesce to one for the $d_0 = 10$ mm layers. To show the evolution process clearly, sketches of the wave patterns and interfacial morphologies at typical moments for the US, IP and AP layers with the same thickness ($d_0 = 20$ mm) are given in figure 5.

3.3. *Instability growth at the early stage*

In this work, we divide qualitatively the instability growth into early and late stages. Here, the early stage refers to the phase at which the instability growth suffers a considerable influence of waves (i.e. a compressibility effect is evident), while the late stage refers to the

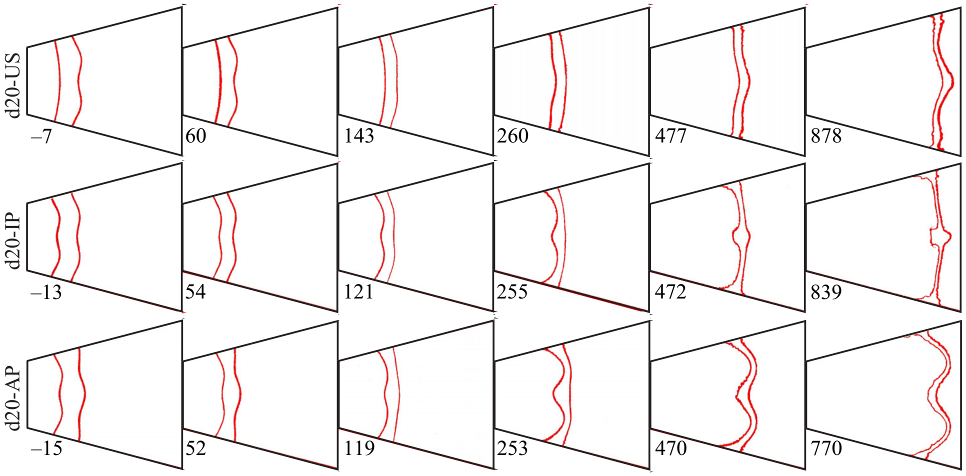

Figure 4. The interface contours extracted from schlieren images at typical moments for the IP, AP and US cases with thickness 20 mm. The unit of numbers is μs.

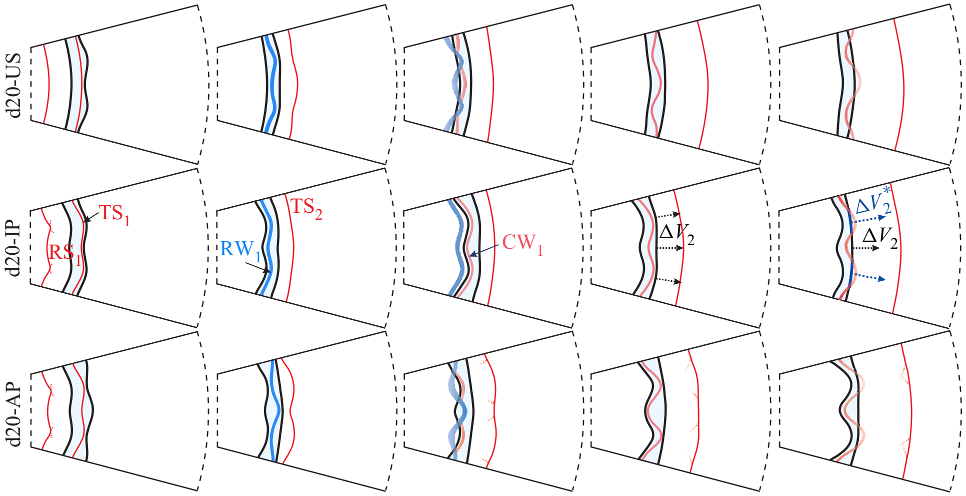

Figure 5. Sketches of the wave patterns and interface morphologies at typical moments for different cases. Here, ΔV_2 (ΔV_2^*) is the velocity of the outer interface immediately after the impact of TS$_1$ (CW$_1$). The other symbols are the same as those in figure 2.

stage at which the wave effects are weak, and interface coupling dominates the instability growth.

3.3.1. *Growth of the inner interface amplitude*

Variations of the amplitude of the inner interface versus time for all cases are plotted in figures 6(*a*,*c*,*e*). For each case, the amplitude of the inner interface first experiences a sudden drop due to shock compression and then grows almost linearly with time before the arrival of RW$_1$. The quasi-linear growth here indicates that geometric divergence produces a negligible influence on the instability growth at the early stage, which is consistent

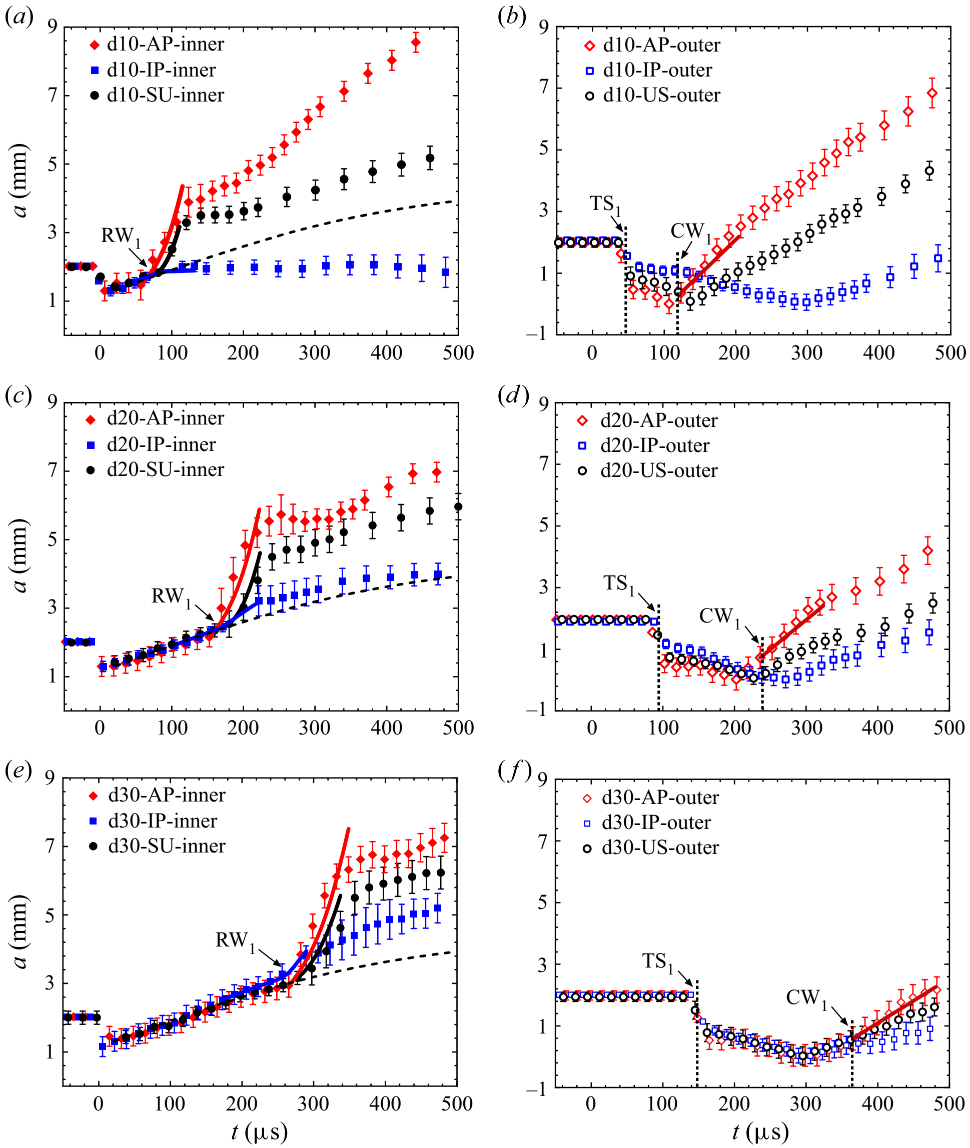

Figure 6. Comparison of the amplitudes of (*a*,*c*,*e*) the inner interface and (*b*,*d*,*f*) the outer interface among different cases. The dashed line refers to the prediction of the Bell–RT model. The bold solid line refers to the prediction of the Bell–RT-m model that considers the interface stretching and RT instability caused by RW_1 in (*a*,*c*,*e*), and to the instability growth caused by CW_1 in (*b*,*d*,*f*). The symbols are the same as those in figure 2.

with the previous finding (Li *et al.* 2020*b*; Zhang *et al.* 2023). The experimental data of the SU layers with various thicknesses from Zhang *et al.* (2023) are also given in figures 6(*a*,*c*,*e*) for comparison. Comparison among the SU, IP and AP cases (the initial inner interface remains the same for the three cases) for the amplitude growth of the inner interface can reveal the influence of phase difference between the two interfaces on the inner interface development. As we can see, for each thickness, the instability growths at the inner interface for the SU, IP and AP cases collapse quite well before the arrival of RW_1, which indicates a negligible interface coupling effect. This can be interpreted from

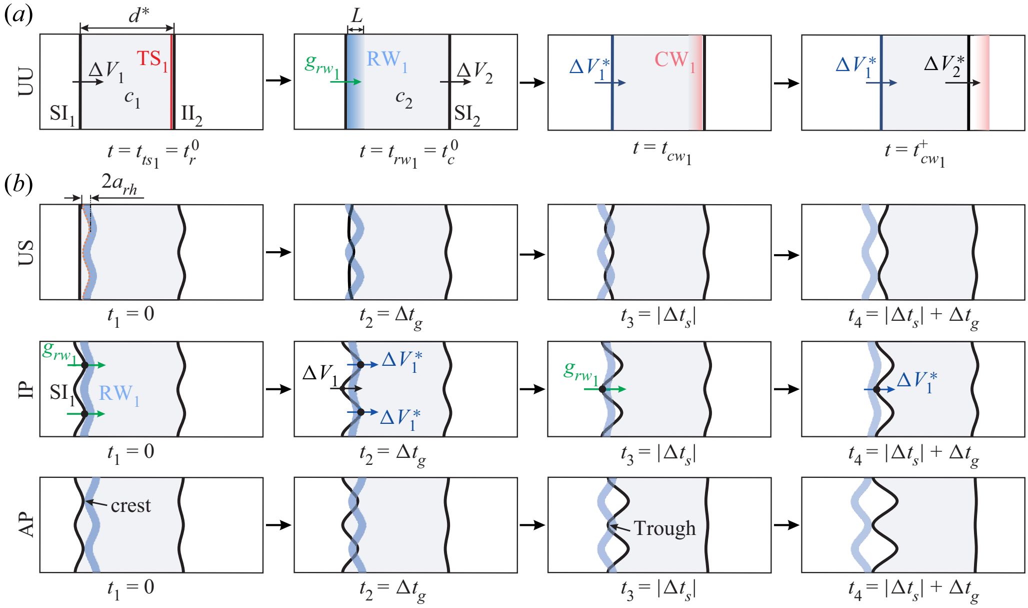

Figure 7. Schematic diagrams showing (*a*) the wave propagations and interface motions for a shock wave impacting a heavy gas layer, and (*b*) the detailed process of the distorted RW_1 passing through the inner interface. Here, d^* is the layer thickness just before TS_1 collides with II_2, ΔV_1 (ΔV_2) is the post-shock velocity of the inner (outer) interface, ΔV_1^* (ΔV_2^*) is the velocity of the inner (outer) interface after the impact of RW_1 (CW_1), L is the distance between the head and tail of RW_1 just before it impacts the inner interface, and c_1 (c_2) denotes the sound speed of the fluid behind TS_1 (RW_1) inside the layer. The symbols are the same as those in figure 2.

the perspective of pressure disturbances. For compressible fluids, the perturbation at one interface feeds through to another interface via pressure disturbance, which propagates at the sound speed and thus cannot cross the reverberating waves (such as RW_1 and CW_1) to influence the other interface. Thus, before the arrival of RW_1, the evolution of the inner interface suffers no influence of the outer interface, and vice versa (i.e. there is no interface coupling effect at this time). This also explains the observation that the classical Bell (1951) theory developed for cylindrical RM instability at a single interface gives a good prediction (dashed line) of the instability growth at the inner interface before the arrival of RW_1 for all cases. When RW_1 arrives, the inner interface presents a much quicker instability growth than the prediction of Bell theory, which indicates that RW_1 promotes the instability growth at the inner interface. It is found that for gas layers with an identical thickness, RW_1 promotes the instability growth to a large extent for the AP case, to a moderate extent for the SU case, and to a small extent for the IP case. In particular, for case d10-IP, the RW_1 event inhibits the instability growth. This implies that the effect of RW_1 on the growth of the inner interface depends heavily on the initial perturbation phases of the two interfaces.

Here, we give a quantitative estimation of the influence of RW_1 on the instability growth, which is crucial for understanding and modelling the instability growth of a fluid layer at the early stage. Since the layer thickness is much smaller than its radius (i.e. $d \ll R$), RW_1 experiences only a subtle change in velocity while propagating inside the layer. Thus the motion of RW_1 can be assumed as that in a planar geometry, as sketched in figure 7(*a*). The time at which TS_1 encounters the outer interface is defined as t_{ts_1}, the time at which RW_1

Case	t_{ts_1}	t_{rw_1}	t_{cw_1}	ΔV_1^*	ΔV_2^*	c_1	c_2	γ	L	Δt_g	g_{rw_1}
d10-UU	45.0	82.2	120.6	123.7	126.1	155.9	154.5	1.11	0.69	4.1	6 440 000
d20-UU	95.2	164.8	240.6	124.7	124.1	156.2	154.7	1.11	1.12	6.6	4 250 000
d30-UU	147.8	250.4	363.3	128.1	123.6	153.3	151.7	1.12	1.54	9.1	3 440 000

Table 2. The key parameters for the interactions of a divergent shock with unperturbed layers of different thicknesses. Here, t_{ts_1} and t_{cw_1} are the times when TS_1 and CW_1 encounter the outer interface, respectively, t_{rw_1} is the time when RW_1 encounters the inner interface, ΔV_1^* (ΔV_2^*) is the velocity of the inner (outer) interface after the impact of RW_1 (CW_1), c_1 (c_2) is the sound speed of the fluid behind TS_1 (RW_1) inside the layer, γ is the specific heat ratio inside the layer, L is the width between the head and tail of RW_1 when it encounters the inner interface, Δt_g is the time duration between the inner interface passing through the head and tail of RW_1, and g_{rw_1} is the average acceleration of the inner interface caused by RW_1. The units are µs, mm, m s^{-1} and m s^{-2} for the time, length, speed and acceleration, respectively.

is generated as t_r^0, and the time at which RW_1 interacts with the shocked inner interface as t_{rw_1}. Then t_{ts_1}, t_r^0 and t_{rw_1} can be estimated by

$$\left.\begin{aligned} t_{ts_1} &= t_r^0 = \frac{d_0}{V_{ts_1}},\\ t_{rw_1} &= \frac{d_0(V_{ts_1} - \Delta V_1 + c_1)}{c_1\, V_{ts_1}} = t_{ts_1} + \frac{d_0}{c_1}\left(1 - \frac{\Delta V_1}{V_{ts_1}}\right), \end{aligned}\right\} \tag{3.3}$$

where c_1 is the sound speed of the gas behind TS_1 inside the layer. According to 1-D gas dynamics theory, the width of RW_1 (defined as the distance between its head and tail) at the moment when it encounters the inner interface is $L = (\gamma + 1)(\Delta V_2 - \Delta V_1)d^*/(2c_1)$, where γ is the specific heat ratio inside the layer, and $d^* = d_0(1 - \Delta V_1/V_{ts_1})$ is the layer thickness at t_{ts_1}. According to Morgan, Likhachev & Jacobs (2016), it can be assumed that RW_1 accelerates the inner interface with a constant acceleration (g_{rw_1}). Then Δt_g (i.e. the acceleration duration) and g_{rw_1} can be calculated by $\Delta t_g = 2L/(2c_1 + \Delta V_1^* - \Delta V_1)$ and $g_{rw_1} = (\Delta V_1^* - \Delta V_1)/\Delta t_g$, respectively, where ΔV_1^* is the velocity of the inner interface after the impact of RW_1. The relevant parameters for the unperturbed layers of different thicknesses are listed in table 2. Note that for a perturbed layer, the interface acceleration caused by RW_1 would induce RT instability, which can evidently promote the instability growth (Liang *et al.* 2020*b*; Liang & Luo 2021*a*).

Besides interface acceleration, RW_1 also stretches the interface, causing a quick increment in interface amplitude (called the interface stretching effect in this work). The parameters listed in tables 1 and 2 enable us to quantify the interface stretching effect. As shown in figure 5, for any of the US, IP or AP cases, after TS_1 collides with the sinusoidal outer interface, a disturbed RW_1 that presents an in-phase perturbation relative to the outer interface is generated immediately. The initial amplitudes of the leading front (a_{rh}^0) and trailing front (a_{rt}^0) of RW_1 can be calculated by

$$\left.\begin{aligned} a_{rh}^0 &= a_{20} + \frac{c_1 - \Delta V_1}{V_{ts_1}}(a_{20} - a_{ts_1}(t_{ts_1})),\\ a_{rt}^0 &= a_{20} + \frac{c_2 - \Delta V_2}{V_{ts_1}}(a_{20} - a_{ts_1}(t_{ts_1})), \end{aligned}\right\} \tag{3.4}$$

where $a_{ts_1}(t_{ts_1})$ is the amplitude of TS_1 at t_{ts_1}. Since there is no theoretical solution for the variation of a rippled shock amplitude in divergent geometry, $a_{ts_1}(t_{ts_1})$ is measured from

Case	$a_{ts_1}(t_{ts_1})$	a^0_{rh}	$a_1(t_{rw_1})$	$a^0_{cw_1}$	$a_2(t_{cw_1})$	Δt_s	Δt_{rw_1}	Δt_{cw_1}	$\dot{a}^{rw}_s$	$\dot{a}_1$	$\dot{a}_2$
d10-US	0	2.56	0	−2.86	0.57	−32.9	36.9	44.4	−13.05	10.00	12.68
d20-US	0	2.57	0	−2.80	−0.07	−33.0	39.5	35.4	−14.00	4.70	10.58
d30-US	0	2.56	0	−2.87	−0.52	−33.4	42.5	29.7	−15.70	1.90	9.80
d10-IP	0.89	2.31	1.84	1.31	1.09	−6.1	10.1	2.9	−7.82	0.37	7.31
d20-IP	0.79	2.35	2.46	2.58	0.14	1.4	8.0	31.6	2.52	5.70	8.00
d30-IP	0.63	2.38	3.28	4.25	−0.37	11.7	20.8	60.9	8.82	9.99	6.94
d10-AP	0.89	−2.81	1.47	6.24	−0.01	54.9	59.0	80.9	12.15	17.35	17.22
d20-AP	0.79	−2.80	2.16	7.57	0.66	63.5	70.1	89.3	12.69	10.93	12.26
d30-AP	0.63	−2.74	2.94	9.08	0.35	74.0	83.2	115.1	13.98	9.07	7.67

Table 3. The relevant parameters for all perturbed layers. Here, $a_{ts_1}(t_{ts_1})$ refers to the amplitude of TS$_1$ at the time t_{ts_1}, a^0_{rh} ($a^0_{cw_1}$) is the initial amplitude of RW$_1$ (CW$_1$), $a_1(t_{rw_1})$ ($a_2(t_{cw_1})$) is the amplitude of the inner (outer) interface at the time t_{rw_1} (t_{cw_1}), Δt_s is the time duration between the moments when the peak and trough of RW$_1$ respectively encounter the inner interface, Δt_{rw_1} (Δt_{cw_1}) is the time duration for RW$_1$ (CW$_1$) passing through the inner (outer) interface, $\dot{a}^{rw}_s$ represents the average growth rate caused by interface stretching, and $\dot{a}_1$ ($\dot{a}_2$) is the growth rate of the inner (outer) interface after the impact of RW$_1$ (CW$_1$). The units are μs, mm and m s^{-1} for the time, length and speed, respectively.

experiment in this work. The calculated values of a^0_{rh} and a^0_{rt} are nearly equal, thus a^0_{rh} can represent approximately the amplitude of RW$_1$ in this work, as listed in table 3. Also, considering that the amplitude of RW$_1$ undergoes only a subtle variation inside the layer, it can be assumed that $a_{rh}(t_{rw_1}) = a^0_{rt}$. As sketched in figure 7(*b*), during the interaction of RW$_1$ with the inner interface, RW$_1$ accelerates first the bubble of the inner interface and then the spike, producing a velocity difference between the tips of the bubble and the spike. This leads to a quick increment in interface amplitude, i.e. the interface stretching effect. The time duration between the moments at which the crest and trough of the leading front of RW$_1$ encounter respectively the inner interface is defined as Δt_s, which can be calculated by

$$\Delta t_s = \frac{2\left(a_1(t_{rw_1}) - a_{rh}\right)}{c_1}. \tag{3.5}$$

Thus the time duration of RW$_1$ passing across the inner interface is $\Delta t_{rw_1} = |\Delta t_s| + \Delta t_g$, as sketched in figure 7(*b*). The amplitude increment caused by the stretching effect (Δa^{rw}_s) and the corresponding average growth rate ($\dot{a}^{rw}_s$) can be estimated respectively by

$$\left.\begin{aligned} \Delta a^{rw}_s &= \frac{\Delta t_s\left(\Delta V_1^* - \Delta V_1\right)}{2}, \\ \dot{a}^{rw}_s &= \frac{\Delta a^{rw}_s}{|\Delta t_s| + \Delta t_g}. \end{aligned}\right\} \tag{3.6}$$

The calculation results for all cases are listed in table 3. It is seen that for the IP (AP) case, the influences of RW$_1$ on the instability growth at the inner interface are the weakest (strongest) due to the shortest (longest) action time.

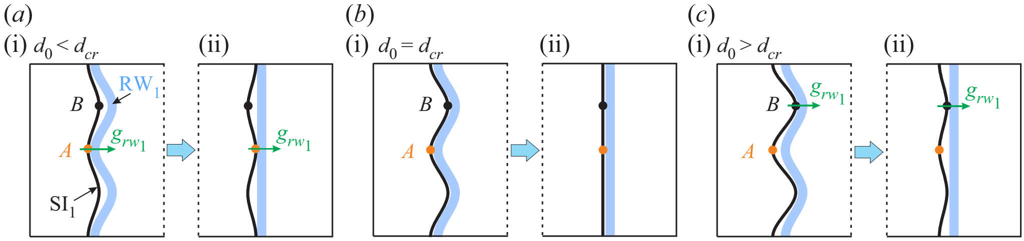

Figure 8. Three situations for (i) the interaction of distorted RW$_1$ with the inner interface in case IP, and (ii) the equivalent diagrams considering RW$_1$ is undisturbed. Here, d_0 refers to the initial layer thickness, d_{cr} is the critical thickness of the layer (where the amplitudes of RW$_1$ and inner interface are equal at the time t_{rw_1}), g_{rw_1} is the average acceleration of the inner interface caused by RW$_1$, and A and B are the points on the tip of the spike and the bubble, respectively. The other symbols are the same as those in figure 2.

To reveal the influence of layer thickness, here we define a critical thickness d_{cr} for the gas layer in which the interface amplitude is equal to the amplitude of RW$_1$ when they meet, i.e. $a_1(t_{rw_1}) = a_{rh}(t_{rw_1})$. There are three possible situations, depending on the layer thickness: $d_0 < d_{cr}$, $d_0 = d_{cr}$ or $d_0 > d_{cr}$. As sketched in figure 8, for $d_0 < d_{cr}$ ($\Delta t_s < 0$), the trough of the inner interface (point A) is first accelerated by RW$_1$, thus both the interface stretching effect and RT instability induce a negative growth rate, i.e. the instability growth is inhibited. For $d_0 = d_{cr}$ ($\Delta t_s = 0$), the trough and crest of the inner interface (points A and B) are accelerated simultaneously by RW$_1$, i.e. the stretching effect disappears. Also, for this situation, RT instability is the weakest due to the shortest duration of RW$_1$ passing through the interface. For $d_0 > d_{cr}$ ($\Delta t_s > 0$), point B is first accelerated by RW$_1$, and both the interface stretching effect and RT instability induce a positive growth rate, i.e. the instability growth is promoted.

Here, we give a quantitative estimation of the critical thickness d_{cr}. Since geometric divergence has a negligible influence on the layer evolution at the early stage (Luo *et al.* 2018), the amplitude of the inner interface just before the impact of RW$_1$ can be approximated as

$$a_1(t_{rw_1}) = a_1^+ + \dot{a}_0\, t_{rw_1}, \tag{3.7}$$

where $a_1^+ = a_{10}(1 - \Delta V_1/V_{ics})$ is the post-shock amplitude, and $\dot{a}_0 \approx 8.0\ \mathrm{m\ s^{-1}}$ (obtained by a linear fit of experimental data) is the post-shock growth rate at the inner interface. Letting $a_1(t_{rw_1}) = a_{rh}(t_{rw_1})$, with (3.10), (3.4) and (3.7), d_{cr} is derived as

$$d_{cr} = \frac{c_1}{\dot{a}_0}\left[(a_{20} - a_{10}) + \frac{a_{10}V_{ts_1}c_1}{V_{ics}\left(V_{ts_1} + c_1 - \Delta V_1\right)} - \frac{c_1 - \Delta V_1}{V_{ts_1} + c_1 - \Delta V_1}\int_0^{t_{ts_1}} \alpha(t)\,\mathrm{d}t\right], \tag{3.8}$$

where $\alpha(t)$ refers to the growth rate of the amplitude of TS$_1$. Since the variation of $\alpha(t)$ in divergent geometry is very complex, for which there is no theoretical solution, it is hard to give a theoretical value for d_{cr}. Here, we consider two limiting cases: for a very thin layer in which the variation of $\alpha(t)$ is negligibly small, there is $\alpha(t) \approx 0$; for a very thick layer in which TS$_1$ has almost recovered to a cylindrical shock at t_{ts_1}, there is $\int_0^{t_{ts_1}} \alpha(t)\,\mathrm{d}t \approx -a_{10}(1 - V_{ts_1}/V_{ics})$. Substituting the relevant parameters into (3.8) (such as case d20-UU in tables 1 and 2), d_{cr} is estimated to be 11.0 mm and 15.8 mm for these two limiting situations, respectively. Hence, for a finite-thickness layer, the critical thickness is within the range $11.0 < d_{cr} < 15.8$ mm. Under the current experimental conditions, if

$d_0 < 11.0$ mm, then the instability growth at the inner interface would be inhibited by RW_1, while if $d_0 > 15.8$ mm, then the instability growth would be promoted. The present analysis explains reasonably the suppression of RW_1 on the instability growth at the inner interface for case d10-IP, in which $d_0 < d_{cr}$.

Taking both RT instability and the interface stretching effect caused by the rarefaction wave into account, recently Zhang *et al.* (2023) proposed a modified Bell–RT model (called the Bell–RT-m model), which is expressed as

$$a(t) = a_0^+ + \dot{a}_0 R_0^2 \int_{t_0^+}^{t} \frac{1}{R^2(t')}\,\mathrm{d}t' + (nA-1)\int_{t_0^+}^{t}\left(\frac{1}{R^2(t')}\int_{t_0^+}^{t'} aR\ddot{R}\,\mathrm{d}t''\right)\mathrm{d}t' + \dot{a}_s^{rw}(t - t_{rw_1}). \tag{3.9}$$

This model has been validated by experiment for the case of a uniform rarefaction wave accelerating a perturbed interface (Zhang *et al.* 2023). The present experimental results provide an opportunity to examine the validity of the model for more complex situations, e.g. a distorted rarefaction wave interacts with a perturbed interface. As can be seen in figures 6(*a*,*c*,*e*), (3.9) that takes an average acceleration ($\ddot{R} = g_{rw_1}$) and an average stretching growth rate ($\dot{a}_s^{rw}$) well reproduces the instability growth caused by RW_1 for most cases. An exception is the d30-AP case, in which the perturbation growth is overestimated. The reason is discussed below. As we know, the RT effect plays a role only when RW_1 accelerates the interface. For case d30-AP, the inner interface presents a relatively large amplitude just before the impact of RW_1, and also its perturbation phase is opposite to that of RW_1. As a result, the passage of RW_1 across the inner interface in case d30-AP lasts a longer period of time than in the other cases. As sketched in figure 7(*b*), for this case the crest of RW_1 has been far away from the inner interface when the trough of RW_1 encounters the inner interface. In the calculation of (3.9), it is thought that RT instability acts on the interface at the whole stage of the interaction of RW_1 with the interface, which is not the case for the real situation. This may be the reason for the overestimation of the instability growth for case d30-AP. It is seen that the inhibition of the instability growth at the inner interface caused by RW_1 in case d10-IP is also reproduced by the Bell–RT-m model. The present analysis suggests that the Bell–RT-m model is valid for cases with various perturbation phases and thicknesses except the AP case with a relatively large thickness.

3.3.2. *Growth of the outer interface amplitude*

Temporal variations of the amplitude of the outer interface for the US, IP and AP cases (the initial outer interface remains the same for the three cases) are given in figures 6(*b*,*d*,*f*). As we can see, the amplitude of the outer interface suffers a sudden drop due to the compression of TS_1. The interaction of the distorted TS_1 with the sinusoidal outer interface here belongs to complex non-standard RM instability (i.e. a rippled shock impacts a perturbed interface), which involves more regimes than the simple non-standard RM instability (i.e. a rippled shock impacts an unperturbed interface) and the conventional standard RM instability (a uniform shock impacts a perturbed interface) (Ishizaki *et al.* 1996; Zou *et al.* 2017, 2019; Li *et al.* 2022*a*). Here, we analyse the perturbation growth caused by TS_1 in the view of baroclinic vorticity, which is a major driving force for the instability growth. Sketches in the first row of figure 5 show the interaction of TS_1 with the outer interface for the US, IP and AP cases. For the IP case, TS_1 is in phase with the outer interface (i.e. there is a small angle between the density gradient across the interface and the pressure gradient at TS_1), thus weaker baroclinic vorticity is deposited at the interface than in the US case. Also, the interface is compressed to a lower extent as compared to the US case. This leads to a slower instability growth at the early stage in the IP case than in the US case. For the AP case, TS_1 is out of phase with the outer interface, thus stronger baroclinic vorticity is deposited at the outer interface than in the US case. Also, the interface is compressed to a larger extent. These lead to a quicker instability growth at the early stage than in the US case. It should be stressed that for the large-thickness layers such as case d30-IP and case d30-AP, TS_1 has recovered to a cylindrical divergent shock just before it arrives at the outer interface, thus the instability growths at the outer interface collapse well before the impact of CW_1, as shown in figure 6(*f*). After the impact of CW_1, the AP case presents a quicker instability growth than in the US case, whereas the IP case presents a slower instability growth. The present results indicate that CW_1 also affect the instability growth.

Similar to RW_1, CW_1 also experiences a subtle change in velocity while propagating inside the layer, thus its motion can be assumed as that in a planar geometry, as sketched in figure 7(*a*). The time at which CW_1 is generated is defined as t_c^0, and the time at which CW_1 interacts with the shocked outer interface is defined as t_{cw_1}. Then t_c^0 and t_{cw_1} can be estimated by

$$\left.\begin{aligned} t_c^0 = t_{rw_1} = t_{ts_1} + \frac{d_0}{c_1}\left(1 - \frac{\Delta V_1}{V_{ts_1}}\right), \\ t_{cw_1} = t_{rw_1} + \frac{d_0}{c_2}\left(1 - \frac{\Delta V_1}{V_{ts_1}}\right)\left(1 + \frac{\Delta V_2 - \Delta V_1}{c_1}\right), \end{aligned}\right\} \tag{3.10}$$

where c_2 is the sound speed of the gas behind RW_1 inside the layer. Note that CW_1 possesses an initial perturbation, and its amplitude can be approximated as

$$a_{cw_1}^0 = a_1(t_{rw_1}) + \frac{a_1(t_{rw_1}) - a_{rh}(t_{rw_1})}{c_1}\left(c_2 + \Delta V_2 - \Delta V_1\right). \tag{3.11}$$

The amplitude of CW_1 can be assumed as constant during the short period of propagation inside the layer, i.e. $a_{cw_1}(t_{cw_1}) \approx a_{cw_1}^0$. As shown in figure 5, after the impact of CW_1, the velocity of the outer interface increases from ΔV_2 to ΔV_2^*. Meanwhile, the outer interface increases continuously in amplitude due to the velocity difference between the tips of the spike and the bubble until CW_1 passes completely across the interface. It should be mentioned that the outer interface is reversing phase during its interaction with CW_1. As we can see, the instability growth at the outer interface is promoted for the US and AP cases in which the CW_1 is out of phase with the initial outer interface, whereas it is inhibited for the IP case in which the CW_1 is in phase with the initial outer interface. The time duration for CW_1 passing through the outer interface can be estimated by $\Delta t_{cw_1} = 2[a_{cw_1}(t_{cw_1}) - a_2(t_{cw_1})]/c_2$. As listed in table 3, the effect of CW_1 on the outer interface for the AP case is much greater than that of the US and IP cases due to its longer action time. Then the influence of CW_1 on the growth of the outer interface can be estimated as $\Delta a_2^{cw} = (\Delta V_2^* - \Delta V_2)\,\Delta t_{cw_1}/2$. The results indicate that the amplitude variation in the US and IP cases is much smaller than that of the AP case. In particular, it is almost equal in size to the spatial resolution of schlieren images and thus can be ignored. We assume that the interface amplitude increases linearly with time during the short stage of the interaction of CW_1 with the outer interface. Thus the growth rate of the outer interface can be obtained by a linear superposition of the growth rate just before the arrival of CW_1 ($\dot{a}_2$, obtained by experimental fitting and listed in table 3) and the average growth rate caused by CW_1 ($\dot{a}^{cw} = (\Delta V_2^* - \Delta V_2)/2$). This gives a good prediction of the amplitude growth of the outer interface at the CW_1-affection stage for the AP case, as shown by the thick solid lines in figures 6(*b*,*d*,*f*). It can be concluded here that the influence of RW_1, TS_1 and CW_1 on the instability growth can be modulated by changing their perturbation phase relative to the interface (i.e. by changing the initial phase difference between the inner and outer interfaces). In particular, as has been found by Zhang *et al.* (2023), the effect of reverberating waves on divergent RM instability is more evident than that in planar and convergent RM instabilities, thus the instability modulation through waves would be more efficient for divergent RM instability.

3.4. *Instability growth at the late stage*

As the waves are away from the interface, the flow near the gas layer is nearly incompressible (i.e. the effect of waves is negligible) and interface coupling becomes evident, which dominates the late-stage instability growth. In particular, for RM instability in a divergent geometry, the gas layer becomes thinner and thinner with time, producing an increasingly strong interface coupling effect. As shown in figure 9, for each thickness, the AP case presents the largest growth rate at late stages, the SU case presents the medium growth rate, and the IP case presents the smallest growth rate. This is ascribed mainly to the various interface coupling effects in these cases. Specifically, for the IP case, the inner and outer interfaces present opposite phases at late stages, thus their evolutions are inhibited by each other due to interface coupling (Mikaelian 1995). For the AP case, the inner and outer interfaces present an identical phase at late stages, and their evolutions are promoted by interface coupling. Thus for the IP case, the perturbation on the inner/outer interface presents a slower instability growth than the SU/US case, but the AP case presents a quicker instability growth than the SU/US case. This finding is consistent qualitatively with that in planar (Liang & Luo 2021*a*, 2022) and convergent (Li *et al.* 2022*a*) RM instabilities. Recently, Matsuoka & Nishihara (2023) also found the dependence of phase difference on the instability growth from the perspective of vortex sheet dynamics. It should be stressed that the instability growth trends for various layer thicknesses are generally similar, which indicates that the layer thickness is a relatively minor factor compared to the phase difference between the two interfaces within the parameter space considered in this work.

Under the incompressible, inviscid, irrotational fluid assumption, Mikaelian (2005) has derived a set of linear equations for RM instability at an arbitrary number (N) of cylindrical layers:

$$(\rho_{i+1}-\rho_i)\frac{\mathrm{d}}{\mathrm{d}t}(R_i\dot{R}_i a_i) = R_i^{n+1}\left(\rho_{i+1}\frac{\mathrm{d}B_{i+1}}{\mathrm{d}t}-\rho_i\frac{\mathrm{d}B_i}{\mathrm{d}t}\right)+(R_i)^{1-n}\left(\rho_{i+1}\frac{\mathrm{d}C_{i+1}}{\mathrm{d}t}-\rho_i\frac{\mathrm{d}C_i}{\mathrm{d}t}\right), \tag{3.12}$$

where

$$\left.\begin{aligned} B_i &= \frac{1}{n\left[R_i^{2n}-(R_{i-1})^{2n}\right]}\left[R_{i-1}^n\frac{\mathrm{d}}{\mathrm{d}t}(R_{i-1}a_{i-1})-R_i^n\frac{\mathrm{d}}{\mathrm{d}t}(R_i a_i)\right],\\ C_i &= B_i(n\to -n). \end{aligned}\right\} \tag{3.13}$$

Here, $i=1,\ldots,N$ refers to the serial number of the cylindrical layer from inside to outside (the thickness of the Nth cylindrical layer tends to infinity), ρ_i is the fluid density in the ith layer, $\dot{R}$ ($\ddot{R}$) is the first (second) derivative of the interface radius (R) with time, and $C_1=B_N=0$. For $N=2$, there is only one interface and the equation

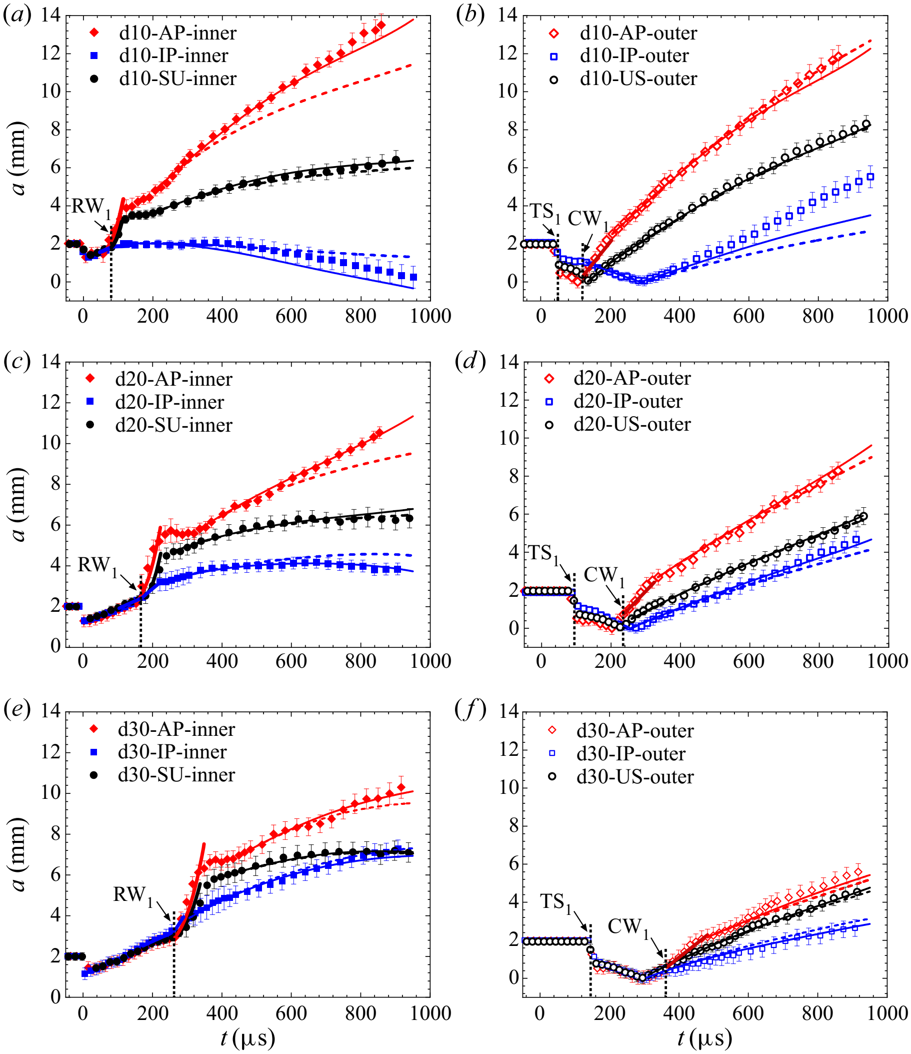

Figure 9. Comparison of the amplitudes of (a,c,e) the inner interface and (b,d,f) the outer interface between experiments and predictions for all cases. The dashed line refers to the prediction of the Bell–RT model that takes the post-wave (RW$_1$ and CW$_1$) growth rate as the initial value; the bold solid line refers to the prediction of the Bell–RT-m model; the thin solid line refers to the prediction of the Bell–RT-C model. The vertical dotted line denotes the times of reverberating waves interacting with the inner and outer interfaces. The symbols are the same as those in figure 2.

reduces to

$$\frac{\mathrm{d}^2 a}{\mathrm{d}t^2} + \frac{2\dot{R}}{R}\frac{\mathrm{d}a}{\mathrm{d}t} - (nA-1)\frac{\ddot{R}}{R}a = 0, \tag{3.14}$$

which is called the Bell (1951) equation. Treating the shock impact as an impulse function (i.e. $\ddot{R} = \delta(t)\,\Delta V$) and then integrating the Bell equation, the interface amplitude at any time t is obtained as

$$a(t) = a_0^+ + \dot{a}_0 R_0^2 \int_{t_0^+}^{t} \frac{1}{R^2(t')}\,\mathrm{d}t' + (nA-1)\int_{t_0^+}^{t}\left(\frac{1}{R^2(t')}\int_{t_0^+}^{t'} a(t'')\,R(t'')\,\ddot{R}(t'')\,\mathrm{d}t''\right)\mathrm{d}t', \tag{3.15}$$

where a_0^+ refers to the post-shock amplitude, t_0^+ to the time just after the shock passage, and $\dot{a}_0$ to the initial growth rate at t_0^+. For brevity, (3.15) is termed the Bell–RT model. It has been demonstrated that the Bell–RT model is able to give a reasonable prediction of the instability growth at a single sinusoidal interface in divergent/convergent geometry (Ding *et al.* 2019; Li *et al.* 2020*b*). For the gas layer considered in this work, there are three cylindrical layers, i.e. $N = 3$. Performing a lengthy algebraic operation of (3.12), the differential equations for the instability growths at the inner and outer interfaces are available, expressed as

$$\left.\begin{aligned} E_1\ddot{a}_1 + F_1\dot{a}_1 + H_1a_1 + K_1\ddot{a}_2 + L_1\dot{a}_2 + P_1a_2 = 0,\\ E_2\ddot{a}_1 + F_2\dot{a}_1 + H_2a_1 + K_2\ddot{a}_2 + L_2\dot{a}_2 + P_2a_2 = 0. \end{aligned}\right\} \tag{3.16}$$

Here, $E_{1/2}, F_{1/2}, H_{1/2}, K_{1/2}, L_{1/2}, P_{1/2}$ are the algebraic expressions of the relevant interface parameters (R, $\dot{R}$, $\ddot{R}$, n, ρ_i), as given in Appendix A. Also, a_1 and a_2 are the amplitudes of the inner and outer interfaces, respectively, and $\dot{a}$ ($\ddot{a}$) is the first (second) derivative of the amplitude with respect to time. Equations (3.16), which involve the interface coupling effect, are termed the Bell–RT-C model in this work. Since it is difficult to derive a theoretical solution for (3.16), here a program is developed to solve numerically the Bell–RT-C model. To verify the reliability of the program, the Bell–RT-C model with a very large azimuthal mode number n for which the two interfaces nearly decouple (Mikaelian 1995, 2005) is solved first. As expected, the Bell–RT-C model gives almost the same prediction as that of (3.15) for each interface in this case, which demonstrates the accuracy of the program.

To the authors' knowledge, the theory of Mikaelian (2005) has never been validated by experiment. A major reason is that it is very difficult to obtain high-fidelity experimental results for RM instability at two or more well-controlled interfaces in a cylindrical geometry. Another reason is that the theory of Mikaelian (2005) is suitable only for the instability growth within the linear regime, which brings more challenge to experiments in which nonlinearity is usually present. We state that the divergent RM instability presents much weaker nonlinearity than the planar and convergent counterparts (Li *et al.* 2020*b*), and thus provides a natural opportunity to examine the validity of the Mikaelian theory. Also, the gas layer in a divergent geometry becomes thinner and thinner with time, producing an increasingly strong interface coupling effect. Hence divergent RM instability at a gas layer considered in this work is an excellent configuration for examining the Bell–RT-C model.

Comparisons between the experiment and the prediction of the Bell–RT-C model for the variations of the amplitudes of the inner and outer interfaces versus time at late stages are given in figure 9, where the prediction of the Bell–RT model (the dashed line) is also given. Note that the parameters of the interfaces for the undisturbed layers ($\dot{R}$ and $\ddot{R}$) are adopted for the mode prediction. The growth rate of the inner/outer interface after the impact of RW$_1$/CW$_1$ ($\dot{a}_1$, $\dot{a}_2$ in table 3) obtained by a linear fit of experimental data is taken as the initial value. After the impact of RW$_1$, the inner interface presents diverse instability growths depending on the phase difference between the inner and outer interfaces. Specifically, for each layer thickness, the instability growth at the inner/outer interface for the AP case is much quicker than that of the SU/US case, whereas the instability growth at the inner/outer interface for the IP case is much slower than in the SU/US case. As the gas layer becomes thinner, the instability growth at the inner interface for the AP case is promoted to a larger extent due to the stronger interface coupling. Nevertheless, for the IP case, the thinner the gas layer, the slower the instability growth at the inner and outer interfaces. It is found that the Bell–RT-C model (thin solid line) well reproduces the instability growths at both the inner and outer interfaces for all layers with different shapes and thicknesses. As far as we know, this is the first experimental confirmation of the Mikaelian theory for cylindrical RM instability at multiple interfaces. The good agreement between theory and experiment for the instability growths at both the inner and outer interfaces demonstrates that interface coupling is a primary factor for the instability growth at late stages. The Bell–RT-C model underestimates the instability growth for case d10-IP. The reason is that for a thinner gas layer, the bubbles at the two interfaces collide with each other earlier, and consequently the two interfaces coalesce into ‘one interface’ (e.g. 449 μs in figure 3), for which the coupling model is no longer valid. The finding in this work indicates that the phase difference between the inner and outer interfaces is a crucial factor for the instability growth at both interfaces of a heavy gas layer from early (through reverberating waves) to late (through interface coupling) stages. This provides a potential way to modulate the growth of divergent RM instability.

4. Conclusions

Experiments on divergent RM instability at various types of perturbed SF_6 layers surrounded by air are conducted in a divergent shock tube. The shock-tube facility is designed based on shock dynamics theory, and its feasibility and reliability have been demonstrated (Li *et al.* 2020*b*; Zhang *et al.* 2023). Benefiting from a novel soap-film technique, the gas layers formed possess controllable shapes and thicknesses. The motion of an unperturbed gas layer in a divergent geometry is described first to facilitate the analysis of the instability at a perturbed layer.

Nine types of perturbed SF_6 layers with different thicknesses and shapes impacted by a cylindrical divergent shock are examined. Specifically, three thicknesses are considered, and for each thickness the layer presents three distinct shapes: unperturbed inner interface and sinusoidal outer interface (case US); sinusoidal inner and outer interfaces that present an identical phase (case IP); sinusoidal inner and outer interfaces that present opposite phases (case AP). The wave evolution and interface deformation are clearly captured by high-quality schlieren images. It is found that the waves reverberating inside the layer, such as RW_1, produce a significant influence on the instability growth at the early stage. Moreover, such an influence depends strongly on the layer shape: RW_1 promotes the instability growth to a large extent for the AP case, to a moderate extent for the SU case, and to a small extent for the IP case. In particular, for case d10-IP, the RW_1 event inhibits the instability growth. Quantitative estimations of the influences of RW_1 and CW_1 on the instability growth are provided, which greatly facilitate the understanding and modelling of divergent RM instability at a fluid layer at the early stage. Also, the layer thickness produces an evident influence on the perturbation growth rate. In particular, for the IP case, a critical thickness is defined and then calculated. If the initial layer thickness is smaller (larger) than the critical thickness, then the instability growth at the inner interface would be inhibited (promoted) by RW_1. This explains reasonably the suppression of RW_1 on the instability growth at the inner interface for case d10-IP, in which $d_0 < d_{cr}$.

As the waves are away from the interface, the compressibility effect is negligible, and interface coupling becomes increasingly strong, which dominates the late-stage instability growth. The interface coupling effect also depends heavily on the layer shape, leading to diverse perturbation growth rates at late stages for the IP, AP and SU cases.

Specifically, the AP case presents the largest growth rate at late stages, the SU case presents the medium growth rate, and the IP case presents the smallest growth rate. Owing to geometric divergence, divergent RM instability presents much weaker nonlinearity and stronger interface coupling than the planar and convergent counterparts. Hence the present experimental results provide a natural opportunity to examine the validity of Mikaelian (2005) theory that was developed for cylindrical RM instability at multiple interfaces within the linear regime. It is found that the Mikaelian theory well reproduces the instability growths at both the inner and outer interfaces for all layers considered in this work. This is the first direct demonstration of the validity of the Mikaelian theory for RM instability at multiple interfaces. The finding in this work indicates that phase difference between the inner and outer interfaces is a crucial factor influencing the instability growth at a gas layer from early (through reverberating waves) to late (through interface coupling) stages. This suggests an efficient way to modulate the growth of divergent RM instability.

Funding. This work was supported by the National Natural Science Foundation of China (nos 12122213, 12072341, 91952205 and 92052108) and the National Key Research and Development Program of China (2022YFF0504500).

Declaration of interests. The authors report no conflict of interest.

Author ORCIDs.
Juchun Ding https://orcid.org/0000-0001-6578-1694;
Liyong Zou https://orcid.org/0000-0003-2702-1816;
Xisheng Luo https://orcid.org/0000-0002-4303-8290.

Appendix A

The relevant parameters in (3.16) are as follows:

$$\left.\begin{aligned} E_1 &= \frac{\rho_1 R_1^2}{n} + \frac{\rho_2 R_1^2}{n}\,\frac{1+\left(\dfrac{R_1}{R_2}\right)^{2n}}{1-\left(\dfrac{R_1}{R_2}\right)^{2n}},\\ E_2 &= \frac{2\rho_2 R_1 R_2 \left(\dfrac{R_1}{R_2}\right)^{n}}{n\left[\left(\dfrac{R_1}{R_2}\right)^{2n}-1\right]}, \end{aligned}\right\} \tag{A1}$$

$$
\left.
\begin{aligned}
F_1 &= \frac{2\rho_1 R_1 \dot{R}_1}{n} + \frac{2\rho_2 R_1 \dot{R}_1}{n} \frac{1 + \left(\dfrac{R_1}{R_2}\right)^{2n}}{1 - \left(\dfrac{R_1}{R_2}\right)^{2n}} \\
&\quad + \rho_2 R_1 \dot{R}_1 \left\{ \frac{\left(\dfrac{R_1}{R_2}\right)^{2n} + 1}{\left[\left(\dfrac{R_1}{R_2}\right)^{2n} - 1\right]^2} + \frac{\left(\dfrac{R_1}{R_2}\right)^{-2n} + 1}{\left[\left(\dfrac{R_1}{R_2}\right)^{-2n} - 1\right]^2} \right\} \\
&\quad - \frac{4\rho_2 R_1 \dot{R}_2 \left(\dfrac{R_1}{R_2}\right)}{\left(\dfrac{R_1}{R_2}\right)^{2n} + \left(\dfrac{R_1}{R_2}\right)^{-2n} - 2} - \rho_2 R_1 \dot{R}_1, \\
F_2 &= \frac{4\rho_2 \dot{R}_1 R_2 \left(\dfrac{R_1}{R_2}\right)^{n}}{n\left[\left(\dfrac{R_1}{R_2}\right)^{2n} - 1\right]} \\
&\quad + \frac{2\rho_2 R_1 \dot{R}_2 \left[\left(\dfrac{R_1}{R_2}\right)^{n} + \left(\dfrac{R_1}{R_2}\right)^{3n}\right] - 2\rho_2 R_1 \dot{R}_1 \left[\left(\dfrac{R_1}{R_2}\right)^{3n-1} + \left(\dfrac{R_1}{R_2}\right)^{n-1}\right]}{\left[\left(\dfrac{R_1}{R_2}\right)^{2n} - 1\right]^2},
\end{aligned}
\right\}
\tag{A2}
$$

$$\left.\begin{aligned}
H_1 &= \frac{\rho_1 R_1 \ddot{R}_1}{n} + \frac{\rho_2 R_1 \ddot{R}_1}{n} \frac{1+\left(\dfrac{R_1}{R_2}\right)^{2n}}{1-\left(\dfrac{R_1}{R_2}\right)^{2n}} \\
&\quad + \rho_2 \left(\dot{R}_1\right)^2 \left\{ \frac{\left(\dfrac{R_1}{R_2}\right)^{2n}+1}{\left[\left(\dfrac{R_1}{R_2}\right)^{2n}-1\right]^2} + \frac{\left(\dfrac{R_1}{R_2}\right)^{-2n}+1}{\left[\left(\dfrac{R_1}{R_2}\right)^{-2n}-1\right]^2} \right\} \\
&\quad - \frac{4\rho_1 \dot{R}_1 \dot{R}_2}{\left(\dfrac{R_1}{R_2}\right)^{2n} + \left(\dfrac{R_1}{R_2}\right)^{-2n} - 2} + (\rho_1-\rho_2) R_1 \ddot{R}_1 - \rho_2 \left(\dot{R}_1\right)^2, \\
H_2 &= \frac{2\rho_2 \ddot{R}_1 R_2 \left(\dfrac{R_1}{R_2}\right)^{n}}{n\left[\left(\dfrac{R_1}{R_2}\right)^{2n}-1\right]} \\
&\quad + \frac{2\rho_2 \dot{R}_1 \dot{R}_2 \left[\left(\dfrac{R_1}{R_2}\right)^{n} + \left(\dfrac{R_1}{R_2}\right)^{3n}\right] - 2\rho_2 \left(\dot{R}_1\right)^2 \left[\left(\dfrac{R_1}{R_2}\right)^{3n-1} + \left(\dfrac{R_1}{R_2}\right)^{n-1}\right]}{\left[\left(\dfrac{R_1}{R_2}\right)^{2n}-1\right]^2},
\end{aligned}\right\} \tag{A3}$$

$$\left.\begin{aligned}
K_1 &= \frac{2\rho_2 R_1 R_2 \left(\dfrac{R_1}{R_2}\right)^{n}}{n\left[\left(\dfrac{R_1}{R_2}\right)^{2n}-1\right]}, \\
K_2 &= \frac{\rho_3 R_2^2}{n} + \frac{\rho_2 R_2^2}{n} \frac{1+\left(\dfrac{R_1}{R_2}\right)^{2n}}{1-\left(\dfrac{R_1}{R_2}\right)^{2n}},
\end{aligned}\right\} \tag{A4}$$

$$\left.\begin{aligned}
L_1 ={}& \frac{4\rho_2 R_1 \dot{R}_2 \left(\dfrac{R_1}{R_2}\right)^n}{n\left[\left(\dfrac{R_1}{R_2}\right)^{2n} - 1\right]} \\
&+ \frac{2\rho_2 R_2 \dot{R}_2 \left[\left(\dfrac{R_1}{R_2}\right)^{n+1} + \left(\dfrac{R_1}{R_2}\right)^{3n+1}\right] - 2\rho_2 \dot{R}_1 R_2 \left[\left(\dfrac{R_1}{R_2}\right)^{3n} + \left(\dfrac{R_1}{R_2}\right)^{n}\right]}{\left[\left(\dfrac{R_1}{R_2}\right)^{2n} - 1\right]^2}, \\
L_2 ={}& \frac{2\rho_3 R_2 \dot{R}_2}{n} + \frac{2\rho_2 R_2 \dot{R}_2}{n} \frac{1 + \left(\dfrac{R_1}{R_2}\right)^{2n}}{1 - \left(\dfrac{R_1}{R_2}\right)^{2n}} \\
&- \rho_2 R_2 \dot{R}_2 \left\{\frac{\left(\dfrac{R_1}{R_2}\right)^{2n} + 1}{\left[\left(\dfrac{R_1}{R_2}\right)^{2n} - 1\right]^2} + \frac{\left(\dfrac{R_1}{R_2}\right)^{-2n} + 1}{\left[\left(\dfrac{R_1}{R_2}\right)^{-2n} - 1\right]^2}\right\} \\
&+ \frac{4\rho_2 \dot{R}_1 R_2 \left(\dfrac{R_1}{R_2}\right)^{-1}}{\left(\dfrac{R_1}{R_2}\right)^{2n} + \left(\dfrac{R_1}{R_2}\right)^{-2n} - 2} + \rho_2 R_2 \dot{R}_2,
\end{aligned}\right\} \tag{A5}$$

$$\left.\begin{aligned}
P_1 &= \frac{2\rho_2 R_1 \ddot{R}_2 \left(\dfrac{R_1}{R_2}\right)^n}{n\left[\left(\dfrac{R_1}{R_2}\right)^{2n} - 1\right]} \\
&\quad + \frac{2\rho_2 \left(\dot{R}_2\right)^2 \left[\left(\dfrac{R_1}{R_2}\right)^{n+1} + \left(\dfrac{R_1}{R_2}\right)^{3n+1}\right] - 2\rho_1 \dot{R}_1 \dot{R}_2 \left[\left(\dfrac{R_1}{R_2}\right)^{3n} + \left(\dfrac{R_1}{R_2}\right)^{n}\right]}{\left[\left(\dfrac{R_1}{R_2}\right)^{2n} - 1\right]^2}, \\
P_2 &= \frac{\rho_3 R_2 \ddot{R}_2}{n} + \frac{\rho_2 R_2 \ddot{R}_2}{n} \frac{1 + \left(\dfrac{R_1}{R_2}\right)^{2n}}{1 - \left(\dfrac{R_1}{R_2}\right)^{2n}} \\
&\quad - \rho_2 \left(\dot{R}_2\right)^2 \left\{ \frac{\left(\dfrac{R_1}{R_2}\right)^{2n} + 1}{\left[\left(\dfrac{R_1}{R_2}\right)^{2n} - 1\right]^2} + \frac{\left(\dfrac{R_1}{R_2}\right)^{-2n} + 1}{\left[\left(\dfrac{R_1}{R_2}\right)^{-2n} - 1\right]^2} \right\} \\
&\quad + \frac{4\rho_2 \dot{R}_1 \dot{R}_2 \left(\dfrac{R_1}{R_2}\right)^{-1}}{\left(\dfrac{R_1}{R_2}\right)^{2n} + \left(\dfrac{R_1}{R_2}\right)^{-2n} - 2} + \rho_2 \left(\dot{R}_2\right)^2 + \left(\rho_2 - \rho_3\right) R_2 \ddot{R}_2.
\end{aligned}\right\} \tag{A6}$$

REFERENCES

ABARZHI, S., BHOWMICK, A., NAVEH, A., PANDIAN, A., SWISHER, N., STELLINGWERF, R. & ARNETT, W. 2019 Supernova, nuclear synthesis, fluid instabilities, and interfacial mixing. *Proc. Natl Acad. Sci.* **116**, 18184–18192.

ARNETT, W.D., BAHCALL, J.N., KIRSHNER, R.P. & WOOSLEY, S.E. 1989 Supernova 1987A. *Annu. Rev. Astron. Astrophys.* **27**, 629–700.

BAI, J.S., ZOU, L.Y., WANG, T., LIU, K., HUANG, W.B., LIU, J.H., LI, P., TAN, D.W. & LIU, C.L. 2010 Experimental and numerical study of shock-accelerated elliptic heavy gas cylinders. *Phys. Rev.* E **82**, 056318.

BALAKUMAR, B.J., ORLICZ, G.C., RISTORCELLI, J.R., BALASUBRAMANIAN, S., PRESTRIDGE, K.P. & TOMKINS, C.D. 2012 Turbulent mixing in a Richtmyer–Meshkov fluid layer after reshock: velocity and density statistics. *J. Fluid Mech.* **696**, 67–93.

BALAKUMAR, B.J., ORLICZ, G.C., TOMKINS, C.D. & PRESTRIDGE, K.P. 2008 Simultaneous particle-image velocimetry-planar laser-induced fluorescence measurements of Richtmyer–Meshkov instability growth in a gas curtain with and without reshock. *Phys. Fluids* **20**, 124103.

BALASUBRAMANIAN, S., ORLICZ, G.C. & PRESTRIDGE, K.P. 2013 Experimental study of initial condition dependence on turbulent mixing in shock-accelerated Richtmyer–Meshkov fluid layers. *J. Turbul.* **14** (3), 170–196.

BELL, G.I. 1951 Taylor instability on cylinders and spheres in the small amplitude approximation. Report no. LA-1321. LANL Los Alamos Scientific Laboratory of the University of California.

BETTI, R. & HURRICANE, O.A. 2016 Inertial-confinement fusion with lasers. *Nat. Phys.* **12** (5), 435–448.

Biamino, L., Jourdan, G., Mariani, C., Houas, L., Vandenboomgaerde, M. & Souffland, D. 2015 On the possibility of studying the converging Richtmyer–Meshkov instability in a conventional shock tube. *Exp. Fluids* **56** (2), 1–5.

Budzinski, J.M., Benjamin, R.F. & Jacobs, J.W. 1994 Influence of initial conditions on the flow patterns of a shock-accelerated thin fluid layer. *Phys. Fluids* **6** (11), 3510–3512.

Chen, C., Xing, Y., Wang, H., Zhai, Z. & Luo, X. 2023 Freeze-out of perturbation growth of single-mode helium–air interface through reflected shock in Richtmyer–Meshkov flows. *J. Fluid Mech.* **956**, R2.

Cohen, R.D. 1991 Shattering of a liquid drop due to impact. *Proc. R. Soc. Lond.* A **435**, 483–503.

Dimonte, G. & Ramaprabhu, P. 2010 Simulations and model of the nonlinear Richtmyer–Meshkov instability. *Phys. Fluids* **22**, 014104.

Ding, J., Li, J., Sun, R., Zhai, Z. & Luo, X. 2019 Convergent Richtmyer–Meshkov instability of heavy gas layer with perturbed outer interface. *J. Fluid Mech.* **878**, 277–291.

Ding, J., Si, T., Chen, M., Zhai, Z., Lu, X. & Luo, X. 2017*a* On the interaction of a planar shock with a three-dimensional light gas cylinder. *J. Fluid Mech.* **828**, 289–317.

Ding, J., Si, T., Yang, J., Lu, X., Zhai, Z. & Luo, X. 2017*b* Measurement of a Richtmyer–Meshkov instability at an air–SF_6 interface in a semiannular shock tube. *Phys. Rev. Lett.* **119** (1), 014501.

Epstein, R. 2004 On the Bell–Plesset effects: the effects of uniform compression and geometrical convergence on the classical Rayleigh–Taylor instability. *Phys. Plasmas* **11** (11), 5114–5124.

Groom, M. & Thornber, B. 2021 Reynolds number dependence of turbulence induced by the Richtmyer–Meshkov instability using direct numerical simulations. *J. Fluid Mech.* **908**, A31.

Guo, X., Cong, Z., Si, T. & Luo, X. 2022 Shock-tube studies of single- and quasi-single-mode perturbation growth in Richtmyer–Meshkov flows with reshock. *J. Fluid Mech.* **941**, A65.

Ishizaki, R., Nishihara, K., Sakagami, H. & Ueshima, Y. 1996 Instability of a contact surface driven by a nonuniform shock wave. *Phys. Rev.* E **53** (6), R5592.

Jacobs, J.W., Jenkins, D.G., Klein, D.L. & Benjamin, R.F. 1995 Nonlinear growth of the shock-accelerated instability of a thin fluid layer. *J. Fluid Mech.* **295**, 23–42.

Jacobs, J.W., Klein, D.L., Jenkins, D.G. & Benjamin, R.F. 1993 Instability growth patterns of a shock-accelerated thin fluid layer. *Phys. Rev. Lett.* **70**, 583–586.

Kuranz, C.C., *et al.* 2018 How high energy fluxes may affect Rayleigh–Taylor instability growth in young supernova remnants. *Nat. Commun.* **9**, 1564.

Li, J., Ding, J., Luo, X. & Zou, L. 2022*a* Instability of a heavy gas layer induced by a cylindrical convergent shock. *Phys. Fluids* **34**, 042123.

Li, J., Ding, J., Si, T. & Luo, X. 2020*a* Convergent Richtmyer–Meshkov instability of light gas layer with perturbed outer surface. *J. Fluid Mech.* **884**, R2.

Li, M., Ding, J., Zhai, Z., Si, T., Liu, N., Huang, S. & Luo, X. 2020*b* On divergent Richtmyer–Meshkov instability of a light/heavy interface. *J. Fluid Mech.* **901**, A38.

Li, X., Fu, Y., Yu, C. & Li, L. 2022*b* Statistical characteristics of turbulent mixing in spherical and cylindrical converging Richtmyer–Meshkov instabilities. *J. Fluid Mech.* **928**, A10.

Liang, Y., Liu, L., Zhai, Z., Ding, J., Si, T. & Luo, X. 2021 Richtmyer–Meshkov instability on two-dimensional multi-mode interfaces. *J. Fluid Mech.* **928**, A37.

Liang, Y., Liu, L., Zhai, Z., Si, T. & Wen, C. 2020*a* Evolution of shock-accelerated heavy gas layer. *J. Fluid Mech.* **886**, A7.

Liang, Y. & Luo, X. 2021*a* On shock-induced heavy-fluid-layer evolution. *J. Fluid Mech.* **920**, A13.

Liang, Y. & Luo, X. 2021*b* Shock-induced dual-layer evolution. *J. Fluid Mech.* **929**, R3.

Liang, Y. & Luo, X. 2022 On shock-induced light-fluid-layer evolution. *J. Fluid Mech.* **933**, A10.

Liang, Y., Zhai, Z., Luo, X. & Wen, C. 2020*b* Interfacial instability at a heavy/light interface induced by rarefaction waves. *J. Fluid Mech.* **885**, A42.

Lindl, J., Landen, O., Edwards, J., Moses, E. & Team, N. 2014 Review of the national ignition campaign 2009–2012. *Phys. Plasmas* **21**, 020501.

Liu, L., Liang, Y., Ding, J., Liu, N. & Luo, X. 2018 An elaborate experiment on the single-mode Richtmyer–Meshkov instability. *J. Fluid Mech.* **853**, R2.

Lombardini, M., Pullin, D.I. & Meiron, D.I. 2014 Turbulent mixing driven by spherical implosions. Part 2. Turbulence statistics. *J. Fluid Mech.* **748**, 113–142.

Luo, X., Zhang, F., Ding, J., Si, T., Yang, J., Zhai, Z. & Wen, C. 2018 Long-term effect of Rayleigh–Taylor stabilization on converging Richtmyer–Meshkov instability. *J. Fluid Mech.* **849**, 231–244.

Matsuoka, C. & Nishihara, K. 2023 Nonlinear interaction of two non-uniform vortex sheets and large vorticity amplification in Richtmyer–Meshkov instability. *Phys. Plasmas* **30**, 062304.

Meshkov, E.E. 1969 Instability of the interface of two gases accelerated by a shock wave. *Fluid Dyn.* **4**, 101–104.

Mikaelian, K.O. 1985 Richtmyer–Meshkov instabilities in stratified fluids. *Phys. Rev.* A **31**, 410–419.

Mikaelian, K.O. 1995 Rayleigh–Taylor and Richtmyer–Meshkov instabilities in finite-thickness fluid layers. *Phys. Fluids* **7** (4), 888–890.

Mikaelian, K.O. 2005 Rayleigh–Taylor and Richtmyer–Meshkov instabilities and mixing in stratified cylindrical shells. *Phys. Fluids* **17**, 094105.

Mohaghar, M., Carter, J., Pathikonda, G. & Ranjan, D. 2019 The transition to turbulence in shock-driven mixing: effects of Mach number and initial conditions. *J. Fluid Mech.* **871**, 595–635.

Morgan, R., Likhachev, O. & Jacobs, J. 2016 Rarefaction-driven Rayleigh–Taylor instability. Part 1. Diffuse-interface linear stability measurements and theory. *J. Fluid Mech.* **791**, 34–60.

Nishihara, K., Wouchuk, J.G., Matsuoka, C., Ishizaki, R. & Zhakhovsky, V.V. 2010 Richtmyer–Meshkov instability: theory of linear and nonlinear evolution. *Phil. Trans. R. Soc.* A **368** (1916), 1769–1807.

Orlicz, G., Balakumar, B., Tomkins, C. & Prestridge, K. 2009 A Mach number study of the Richtmyer–Meshkov instability in a varicose, heavy-gas curtain. *Phys. Fluids* **21**, 064102.

Orlicz, G.C., Balasubramanian, S. & Prestridge, K.P. 2013 Incident shock Mach number effects on Richtmyer–Meshkov mixing in a heavy gas layer. *Phys. Fluids* **25**, 114101.

Plesset, M.S. 1954 On the stability of fluid flows with spherical symmetry. *J. Appl. Phys.* **25**, 96–98.

Prestridge, K., Orlicz, G., Balasubramanian, S. & Balakumar, B.J. 2013 Experiments of the Richtmyer–Meshkov instability. *Phil. Trans. R. Soc.* A **371**, 20120165.

Prestridge, K., Rightley, P.M., Vorobieff, P., Benjamin, R.F. & Kurnit, N.A. 2000 Simultaneous density-field visualization and PIV of a shock-accelerated gas curtain. *Exp. Fluids* **29**, 339–346.

Ranjan, D., Niederhaus, J.H.J., Oakley, J.G., Anderson, M.H., Bonazza, R. & Greenough, J.A. 2008 Shock–bubble interactions: features of divergent shock-refraction geometry observed in experiments and simulations. *Phys. Fluids* **20**, 036101.

Rayleigh, Lord 1883 Investigation of the character of the equilibrium of an incompressible heavy fluid of variable density. *Proc. Lond. Math. Soc.* **14**, 170–177.

Reese, D.T., Ames, A.M., Noble, C.D., Oakley, J.G. & Bonazza, R. 2018 Simultaneous direct measurements of concentration and velocity in the Richtmyer–Meshkov instability. *J. Fluid Mech.* **849**, 541–575.

Richtmyer, R.D. 1960 Taylor instability in shock acceleration of compressible fluids. *Commun. Pure Appl. Maths* **13**, 297–319.

Rightley, P.M., Vorobieff, P., Martin, R. & Benjamin, R.F. 1999 Experimental observations of the mixing transition in a shock-accelerated gas curtain. *Phys. Fluids* **11**, 186–200.

Samtaney, R., Ray, J. & Zabusky, N.J. 1998 Baroclinic circulation generation on shock accelerated slow/fast gas interfaces. *Phys. Fluids* **10**, 1217–1230.

Schilling, O. & Latini, M. 2010 High-order WENO simulations of three-dimensional reshocked Richtmyer–Meshkov instability to late times: dynamics, dependence on initial conditions, and comparisons to experimental data. *Acta Math. Sci.* **30B**, 595–620.

Sewell, E.G., Ferguson, K.J., Krivets, V.V. & Jacobs, J.W. 2021 Time-resolved particle image velocimetry measurements of the turbulent Richtmyer–Meshkov instability. *J. Fluid Mech.* **917**, A41.

Shankar, S.K. & Lele, S.K. 2013 Numerical investigation of turbulence in reshocked Richtmyer–Meshkov unstable curtain of dense gas. *Shock Waves* **24**, 79–95.

Sun, R., Ding, J., Zhai, Z., Si, T. & Luo, X. 2020 Convergent Richtmyer–Meshkov instability of heavy gas layer with perturbed inner surface. *J. Fluid Mech.* **902**, A3.

Taylor, G. 1950 The instability of liquid surfaces when accelerated in a direction perpendicular to their planes. I. *Proc. R. Soc. Lond.* A **201**, 192–196.

Tomkins, C., Kumar, S., Orlicz, G. & Prestridge, K. 2008 An experimental investigation of mixing mechanisms in shock-accelerated flow. *J. Fluid Mech.* **611**, 131–150.

Tomkins, C.D., Balakumar, B.J., Orlicz, G., Prestridge, K.P. & Ristorcelli, J.R. 2013 Evolution of the density self-correlation in developing Richtmyer–Meshkov turbulence. *J. Fluid Mech.* **735**, 288–306.

Vandenboomgaerde, M., Rouzier, P., Souffland, D., Biamino, L., Jourdan, G., Houas, L. & Mariani, C. 2018 Nonlinear growth of the converging Richtmyer–Meshkov instability in a conventional shock tube. *Phys. Rev. Fluids* **3**, 014001.

Wang, H., Wang, H., Zhai, Z. & Luo, X. 2022 Effects of obstacles on shock-induced perturbation growth. *Phys. Fluids* **34** (8), 086112.

Wang, M., Si, T. & Luo, X. 2013 Generation of polygonal gas interfaces by soap film for Richtmyer–Meshkov instability study. *Exp. Fluids* **54**, 1427.

WONGA, M.L. & LELEA, S.K. 2017 High-order localized dissipation weighted compact nonlinear scheme for shock- and interface-capturing in compressible flows. *J. Comput. Phys.* **339**, 179–209.

YANG, J., KUBOTA, T. & ZUKOSKI, E.E. 1993 Application of shock-induced mixing to supersonic combustion. *AIAA J.* **31**, 854–862.

ZHAI, Z., LIU, C., QIN, F., YANG, J. & LUO, X. 2010 Generation of cylindrical converging shock waves based on shock dynamics theory. *Phys. Fluids* **22**, 041701.

ZHAN, D., LI, Z., YANG, J., ZHU, Y. & YANG, J. 2018 Note: a contraction channel design for planar shock wave enhancement. *Rev. Sci. Instrum.* **89**, 056104.

ZHANG, D., DING, J., SI, T. & LUO, X. 2023 Divergent Richtmyer–Meshkov instability on a heavy gas layer. *J. Fluid Mech.* **959**, A37.

ZHANG, Q., DENG, S. & GUO, W. 2018 Quantitative theory for the growth rate and amplitude of the compressible Richtmyer–Meshkov instability at all density ratios. *Phys. Rev. Lett.* **121**, 174502.

ZHANG, Q. & SOHN, S.I. 1997 Nonlinear theory of unstable fluid mixing driven by shock wave. *Phys. Fluids* **9**, 1106–1124.

ZOU, L., AL-MAROUF, M., CHENG, W., SAMTANEY, R., DING, J. & LUO, X. 2019 Richtmyer–Meshkov instability of an unperturbed interface subjected to a diffracted convergent shock. *J. Fluid Mech.* **879**, 448–467.

ZOU, L., LIU, J., LIAO, S., ZHENG, X., ZHAI, Z. & LUO, X. 2017 Richtmyer–Meshkov instability of a flat interface subjected to a rippled shock wave. *Phys. Rev.* E **95** (1–1), 013107.